OUKA
The University of Osaka
Institutional Knowledge Archive

Title	Four types of missense mutations in the VPS13A gene for VPS13A disease
Author(s)	林, 星
Citation	大阪大学, 2026, 博士論文
Version Type	VoR
URL	https://doi.org/10.18910/105605
rights	
Note	

The University of Osaka Institutional Knowledge Archive : OUKA

https://ir.library.osaka-u.ac.jp/

The University of Osaka

Four types of missense mutations in the *VPS13A* gene for *VPS13A* disease

（*VPS13A* 疾患における *VPS13A* 遺伝子のミスセンス変異には四種のタイプが存在する）

大阪大学大学院生命機能研究科

免疫学フロンティア研究センター 免疫・生化学

林　星

2026 年 3 月　博士学位論文

Abstract

Four types of missense mutations in the *VPS13A* gene for *VPS13A* disease
（*VPS13A* 疾患における *VPS13A* 遺伝子のミスセンス変異には
四種のタイプが存在する）

Xing Lin

VPS13A is a conserved intracellular lipid transporter comprising over 3,000 amino acids. Mutations in VPS13A cause *VPS13A* disease, a neurodegenerative disorder characterized by chorea and abnormal erythrocyte morphology. VPS13A forms a complex with the membrane protein XK to mediate ATP-induced phospholipid scrambling in the plasma membrane. Here, I established a mouse cell system expressing full-length VPS13A and analyzed its interaction with XK. Mutagenesis revealed that VPS13A binds XK via its C-terminal β-strand and the β-hairpin in XK's central region --- an interaction essential for scramblase activity. The XK paralog XKR2, which shares a similar β-hairpin, also binds to VPS13A and supports scrambling. I generated ten VPS13A variants corresponding to patient mutations and classified them into four groups: (1) L67P, I90K, and W2453R, which markedly reduced expression; (2) A1091P and M3080R, which were expressed normally but lost scramblase activity; (3) S1446P, Y2713C, Q2689H, and R3084H, which modestly reduced expression or activity; and (4) I2763R mutant, which exerted a dominant effect, altering cell size and disrupting the endoplasmic reticulum independently of XK. These findings clarify the molecular basis of VPS13A–XK interaction, classify the effects of disease mutations, and reveal an unexpected dominant role for a VPS13A variant.

Contents

1. General introduction 1

1.1. Asymmetrically distribution of phospholipids 1

1.2. Purinergic P2X receptors 2

2. Introduction 4

3. Results 6

3.1. VPS13A–XK complex in ATP-induced PtdSer exposure 6

3.2. Interaction between XK's β-hairpin and the C-terminal domain of VPS13A 7

3.3. Ability of XKR2 to respond to ATP for PtdSer exposure 8

3.4. Missense mutations in VPS13A 9

3.5. Giant cell morphology of I2763R-expressing cells 11

3.6. Damaged and fragmented ER in I2763R mutant 12

4. Discussion 14

5. Materials and methods 18

5.1. Cell lines, antibodies, and reagents 18

5.2. Plasmids 19

5.3. Cell transformation 20

5.4. Gene editing 21

5.5. Preparation of whole-cell lysates and membrane fractions 21

5.6. SDS-PAGE, BN-PAGE, and western blotting 22

5.7. Flow cytometry and ATP-induced PtdSer exposure 23

5.8. Confocal microscopy and cell size estimation 24

5.9. Electron microscopy 24

5.10. AlphaFold-based predictions 25

5.11. Statistics 25

6. Figures 27

Figure 1. Requirement of the C-terminal domain of VPS13A for ATP-induced PtdSer exposure 27

Figure 2. Interaction between mouse VPS13A and XK 29

Figure 3. Interaction of XKR2 with VPS13A and its ability to support ATP-induced PtdSer exposure 31

Figure 4. Characterization of VPS13A missense mutations 33

Figure 5. Characterization of VPS13A I2763R mutant 35

Figure 6. Damaged ER in cells expressing the I2763R VPS13A mutant 36

Figure 7. Pathological missense mutations in the mouse VPS13A 38

7. Tables 39

Table 1. Summary of mouse VPS13A mutants harboring the corresponding human mutations 39

8. Supplementary Figures 40

Figure S1. Comparison of the activity of internally mCherry-tagged VPS13A and intact VPS13A in supporting ATP-stimulated P2X7-mediated PtdSer exposure 40

Figure S2. Knob-like structure in the C-terminal PH region of VPS13A 41

Figure S3. Plasma membrane localization of XK mutants 42

Figure S4. Amino acid sequence alignment of the mouse XKR family 43

Figure S5. Expression vector construction for mouse VPS13A mutants 44

Figure S6. The conserved C-terminal region of the VPS13 family 46

Figure S7. Conservation of essential residues between VPS13A and VPS13C 47

Figure S8. Strong hydrophobic interaction I90 and W2453 with surrounding residues 48

9. Supplementary Tables 49

Table S1. Primers used for deleting mCherry from human VPS13A^mCherry 49

Table S2. Primers used for mutagenesis of mouse VPS13A 50

Table S3. Primers used for mutagenesis of mouse XK 51

10. References 52

11. Research achievements 59

12. Acknowledgements 59

1. General introduction

1.1. Asymmetrically distribution of phospholipids

In eukaryotic cells, the plasma membrane comprises a lipid bilayer that separates the cell from its environment. Organelles such as the endoplasmic reticulum (ER), nucleus, mitochondria, and lysosomes are enclosed by lipid bilayers that isolate their lumens from the cytosol (1). The major constituents of lipid bilayers include phospholipids such as phosphatidylcholine (PtdCho), phosphatidylethanolamine (PtdEtn), phosphatidylserine (PtdSer), phosphatidylinositol (PtdIns), and sphingomyelin (SM) (2). Glycerophospholipids are synthesized in the ER (3), whereas most SM is synthesized in the Golgi apparatus (4). Lipid composition varies between plasma membranes and intracellular organelles (1). Because phospholipids are amphiphilic, they spontaneously form bilayers with inwardly oriented hydrophobic acyl chains. Variations in acyl chain length and unsaturation influence membrane curvature (2). Cells exploit these properties by asymmetrically distributing phospholipids between the two leaflets of the bilayer (5, 6) to maintain membrane integrity and function.

In the plasma membrane, PtdSer and PtdEtn are usually confined to the cytoplasmic inner leaflet, a distribution maintained by P4-type ATPases ATP11A and ATP11C, which actively flip these phospholipids inward in an ATP-dependent manner (6-8). This asymmetry is disrupted within a short span in processes such as apoptosis, blood clotting, cell fusion, and inflammation, during which PtdSer exposure on the exoplasmic cell surface serves as a signaling cue or enzyme activator (6, 9). However, since the hydrophilic head group of phospholipids has difficulties in moving through the hydrophobic bilayer, it takes a long time to spontaneously destroy the established

asymmetry even if flippases are inactivated (6). Phospholipid scrambling, the ATP-independent bidirectional and nonselective translocation of lipids between bilayer leaflets, is therefore mediated by scramblases. Three types of plasma membrane scramblases have been identified: TMEM16F, XKR8, and TMEM63B (6, 10, 11). TMEM16F functions as a Ca^{2+}-dependent scramblase responsible for PtdSer exposure in activated platelets (12), whereas XKR8 acts as a caspase-dependent scramblase that mediates PtdSer exposure during apoptosis (13).

1.2. Purinergic P2X receptors

Purinergic P2X receptors are ligand-gated ion channels that are activated by extracellular ATP and mediate the flux of cations, including Na^+, Ca^{2+}, and K^+ (14, 15). In contrast to metabotropic P2Y receptors, which are G protein–coupled and exhibit mixed nucleotide selectivity, P2X receptors are ionotropic receptors that preferentially respond to ATP and are largely unresponsive to other nucleotides (16). P2X receptors are widely expressed across mammalian cell types and play essential roles in diverse physiological processes, including modulation of synaptic transmission in neurons and regulation of inflammatory cytokine production in immune cells such as macrophages (15, 17).

The P2X receptor family comprises seven members (P2X1–P2X7), which assemble as homo- or heterotrimeric complexes (15). Among these, P2X7—encoded by the human *P2RX7* gene—is unique in that it forms only homotrimers and possesses an unusually long cytoplasmic C-terminal domain enriched in regulatory motifs (14, 15). Unlike other P2X receptors, which are activated by relatively low ATP concentrations (10–100 μM), P2X7 has a low affinity for ATP and requires high extracellular ATP concentrations

(>100 μM) for activation (18). Such ATP levels are typically generated during necrotic cell death or inflammatory conditions (19), leading to the characterization of P2X7 as a "danger sensor" (20).

Activation of P2X7 triggers a wide range of downstream signaling events (16). In the central nervous system, P2X7 signaling has been described as a double-edged sword: transient activation may confer neuroprotective effects, whereas sustained activation promotes neuroinflammation and tissue damage (18). These observations underscore the complex physiological and pathophysiological roles of P2X7 signaling.

2. Introduction

VPS13A, vacuolar protein sorting 13 homolog A, is a large cytoplasmic protein that belongs to the bridge-like lipid transporter (BLTP) family. It is thought to mediate the directional transfer of phospholipids between organelles, including ER, mitochondria, plasma membrane, and lipid droplets (21, 22). Human VPS13A consists of 3,174 amino acids and contains an N-terminal chorein domain and an extensive β-sheet region with a highly hydrophobic interior (23). Its C-terminal region harbors several domains: a VPS13 adaptor-binding domain (VAB), aberrant pollen transmission 1 domain (APT1), autophagy-related protein C-terminal domain (ATG_C), and pleckstrin homology domain (PH), which mediate interactions with target membranes or adaptor proteins (23, 24). Loss-of-function mutations in the *VPS13A* gene, including deletions and missense variants, cause *VPS13A* disease (historically referred to as chorea-acanthocytosis), a rare autosomal recessive neurodegenerative disorder (22, 25).

Although extracellular ATP concentrations are typically low (~30 nM) compared to intracellular levels (~4 mM) (26), ATP can reach hundreds of micromolar levels in inflamed tissues or tumors due to its release from necrotic cells. In these settings, ATP binds to the P2X7 receptor on $CD25^{+}$ regulatory T-cells and macrophages, triggering PtdSer exposure (15, 16). In a CRISPR–Cas9 screen for genes involved in ATP-induced PtdSer exposure in T cells, the VPS13A–XK complex was previously identified as a scramblase activated downstream of ATP-engaged P2X7 (27). The shared clinical features of *XK* disease (McLeod syndrome) and *VPS13A* disease prompted several groups to report the physical and functional interactions between XK and VPS13A (28-31). Furthermore, by transiently expressing internally Halo- or mCherry-tagged human

VPS13A or a GFP-tagged C-terminal fragment of VPS13A in COS or HEK293T cells, Park et al. (29) and Guillén-Samander et al. (30) showed that VPS13A interacts with XK via the C-terminal PH domain.

In this study, I established stable mouse cell lines expressing intact mouse VPS13A and demonstrated that its complex formation with XK is required for ATP-stimulated lipid scrambling. I also identified mouse XKR2, a previously identified orphan XKR family member, as a VPS13A-binding partner that supports lipid scrambling. Finally, using stable transformants expressing mouse VPS13A variants corresponding to patient-derived missense mutations, I found that three mutations impaired protein synthesis or stability, whereas two specifically compromised PtdSer-scramblase activity. Notably, one mutant not only reduced protein expression and scramblase activity but also induced a novel phenotype characterized by enlarged cell size and delayed growth, revealing an additional XK-independent role for VPS13A in cellular physiology.

3. Results

3.1. VPS13A–XK complex in ATP-induced PtdSer exposure

Park et al. (29) previously reported an elongated VPS13A structure predicted by AlphaFold 2.1, in which four overlapping VPS13A segments were individually modeled and assembled into a full-length structure using ChimeraX. The XK model, also predicted by AlphaFold, was aligned with the PH region of VPS13A.

AlphaFold 3 has increased the size limit for structure prediction to 5,000 amino acids and enables the modeling of protein complexes (32), which enabled me to model the structure of full-length VPS13A in complex with XK. When mouse VPS13A and XK sequences were submitted to the AlphaFold 3 server, the resulting complex structure (Figure 1A) was markedly different from the human VPS13A reported by Park et al. (29). The predicted VPS13A structure appeared more compact and bent, suggesting that N- or C-terminal truncations may yield conformations distinct from those of the intact molecule.

GFP-tagged human VPS13A (hVPS13A^GFP), with GFP inserted between codons 1359 and 1360, has been shown to complement *Vps13a* deficiency in yeast (33). In *Tmem16f*$^{-/-}$*P2rx7*$^{-/-}$ mouse WR19L cell (*DKO*) transformants expressing P2X7, treatment with 500 μM ATP induced PtdSer exposure within 5 min at 4 °C (Figure S1) (27). This effect was abolished in *Vps13a*-knockout cells, confirming that VPS13A is required for ATP-stimulated P2X7-mediated PtdSer exposure. Stable expression of full-length human or mouse VPS13A under the control of the human *EF-1α* promoter rescued scramblase activity, whereas hVPS13A^mCherry did not (Figure S1).

To elucidate the molecular mechanism by which the VPS13A–XK complex supports phospholipid scrambling, I generated stable cell lines expressing wild-type or mutant mouse VPS13A or XK in *Vps13a*-null or *Xk*-null cell lines.

3.2. Interaction between XK's β-hairpin and the C-terminal domain of VPS13A

XK, but not XKR8, contains a β-hairpin in its central cytoplasmic region (27), a motif that often mediates protein-protein interactions (34, 35). Two groups (29, 30) demonstrated that this β-hairpin binds to the C-terminal domain of human VPS13A using transient overexpression in COS or 293T cells of GFP-tagged truncated VPS13A or internally mCherry- or Halo-tagged VPS13A. However, the transient overexpression of large or membrane proteins frequently leads to protein aggregation (36).

To test the role of this interaction in scramblase activity, I expressed wild-type mouse VPS13A or C-terminally truncated mutants [R3127* and E3136Vfs*6 (referred to as R3127Δ and E3136Δ, respectively)], corresponding to patient variants (37, 38) in *Vps13a*$^{-/-}$*DKO*-P2X7 cells. SDS-PAGE analysis showed that the mutant proteins were stably expressed, although at significantly reduced levels compared with wild-type VPS13A (Figure 1B). Blue native (BN)-PAGE detected wild-type VPS13A at ~700 kDa in membrane fractions, which was absent in non-transformed or mutant-transformed cells (Figure 1C). Immunoblotting with anti-XK Ab detected a 250 kDa band in VPS13A-non-transformed cells. Given that detergent-solubilized membrane proteins often migrate larger than their expected size in BN-PAGE (39), this band likely represents the monomeric form of the XK protein. In cells expressing wild-type but not mutant VPS13A, XK displayed an additional band at ~720 kDa, which likely represents the VPS13A–XK complex (Figure 1C).

When these transformants were treated with ATP, only those expressing wild-type VPS13A showed PtdSer exposure (Figure 1D), demonstrating that the C-terminal 31 residues of VPS13A are essential for its expression and scramblase activity at the plasma membrane. Structural modeling suggests that the C-terminal PH region of 100 amino

acids (position 3067-3166) forms a knob-like structure comprising one α-helix segment (position 3146-3160) and two clusters of β-strands (β–α–β) stabilized by hydrophobic contacts (V3071 with I3152; I3114 and L3120 with L3153) (Figure S2).

A close examination of the interaction interface between XK and VPS13A revealed that the XK's β-hairpin structure interacts with β-strands in the C-terminal region of VPS13A via specific hydrogen bonds (mouse XK residues E119 and E121 with mouse VPS13A residues R3121 and R3119, respectively) (Figure 2A). To test this, mouse XK residues E119 and/or E121 were mutated to alanine in C-terminally monomeric enhanced GFP (mEGFP)-tagged XK and introduced into *Xk*-null *DKO*-P2X7 cells. As shown in Figure 2B and Figure S3, wild-type and mutant XK were expressed and localized at the plasma membrane. BN-PAGE and functional analyses demonstrated that single E119A or E121A mutants still formed complexes with VPS13A and supported ATP-induced PtdSer exposure as wild-type. However, the double mutant (DM; E119A/E121A) failed to form a complex with VPS13A and could not mediate phospholipid scrambling (Figure 2C and 2D). Thus, the interactions between the XK β-hairpin residues E119 and E121 and the VPS13A C-terminal residues R3121 and R3119 are essential for the assembly of the VPS13A–XK complex and scramblase activity at the plasma membrane.

3.3. Ability of XKR2 to respond to ATP for PtdSer exposure

XKR2, encoded by *Xkrx*, is an orphan member of the XKR family with an unknown function (6, 40). Mouse XKR2 consists of 449 amino acids and shares 38.5% sequence identity with the 446-amino acid XK protein, including the conservation of the β-hairpin structure (Figure S4). The predicted tertiary structure of XKR2 was highly similar to that

of XK (Figure 3A). In contrast with *Xk* gene, *Xkrx* gene is hardly expressed in WR19L cells (GEO GSE181171).

When expression vectors encoding mEGFP-tagged mouse XK or XKR2 were introduced into *Xk*-null *DKO*-P2X7 cells, the amount of expressed XKR2 protein was significantly lower than that of XK (Figure 3B). However, both XK and XKR2 were localized to the plasma membrane (Figure 3C). Suzuki et al. (41) previously found that XKR8 requires Basigin or Neuroplastin as a chaperone to be expressed in the plasma membrane. The abundant expression of XK, but not XKR2, suggests that the chaperone required for XKR2 is insufficient in WR19L and WR19L-derived cells. Remarkably, even this limited amount of XKR2 recruited VPS13A to the membrane fraction, as revealed by BN-PAGE (Figure 3D). While most exogenously expressed XK proteins were not associated with VPS13A, approximately 50% of XKR2 appeared to form a complex with VPS13A (Figure 3D). Consistent with this, XKR2 supported ATP-stimulated PtdSer exposure (Figure 3E).

3.4. Missense mutations in VPS13A

Nine missense mutations in human VPS13A (L67P, I90K, A1095P, S1452P, W2460R, Y2721C, I2771R, M3088R, and R3092H) have been reported in patients with *VPS13A* disease (38, 42-46). In addition, a VPS13A missense mutation (Q2697H) has been registered in the Human Gene Mutation Database (HGMD, https://www.hgmd.cf.ac.uk) as one of the 140 missense mutations identified in patients with schizophrenia (47).

Mouse VPS13A share 84% identity in amino acid sequence with human VPS13A, and human VPS13A compensate the null-mutation of mouse *Vps13a* gene in mouse cells

(Figure S1) indicating that VPS13A has no species-specificity between human and mouse at least in ATP-induced scramblase activity. To assess the functionality of the VPS13A variants found in patients, ten corresponding mutants (nine from patients with *VPS13A* disease and one from schizophrenia) were introduced into the mouse *Vps13a* cDNA using PCR-based site-directed mutagenesis (Figure S5). The mutant cDNAs were expressed under the *EF-1α* promoter (48) and introduced into *Vps13a*$^{-/-}$*DKO*-P2X7 cells via electroporation. Stable transformants were isolated by limiting dilution, and more than ten individual clones per mutant were screened by western blotting for VPS13A expression. The highest-expressing clones of each mutant were selected for analysis, revealing four types of mutations (Table 1).

In the first type of mutants, three variants (L67P, I90K, and W2453R) were expressed at barely detectable levels (Figure 4A), and their corresponding transformants failed to exhibit ATP-induced PtdSer exposure (Figure 4B), indicating that these mutations destabilized VPS13A or severely impaired its expression.

The second type of mutants (S1446P, Q2689H, Y2713C and R3084H) had less impact on expression and/or function. In particular, two mutants (Q2689H and R3084H) were expressed at levels comparable to those of wild-type VPS13A (Figure 4A) and supported ATP-induced PtdSer exposure (Figure 4C) by forming complexes with XK (Figure 4D), although complex formation was less efficient for Q2689H. Y2713C was expressed at ~40% of the wild-type levels (Figure 4A), yet retained ATP-induced PtdSer exposure and VPS13A–XK complex formation (Figure 4C and 4D).

In contrast, A1091P and M3080R mutants were expressed at higher levels than Y2713C (Figure 4A) but failed to support ATP-induced PtdSer exposures (Figure 4C). VPS13A recruitment to the plasma membrane is dependent on XK (27). SDS-PAGE of

membrane fractions showed that the A1091P protein was present at ~50% of the wild-type VPS13A level, comparable to that of Y2713C (Figure 4D, bottom). However, BN-PAGE revealed that the A1091P–XK complex was markedly larger than the wild-type VPS13A–XK or Y2713C–XK complexes (Figure 4D, top panel), suggesting that A1091P induced aberrant aggregation. Conversely, the M3080R mutant was recruited to the membranes less efficiently (25.6% of wild-type VPS13A) and showed little or no detectable interaction with XK (Figure 4D).

Taken together, these findings suggest that the disease phenotypes observed in patients carrying mutations corresponding to the mouse VPS13A A1091P or M3080R variants can be attributed to the impaired phospholipid scrambling activity of the VPS13A–XK complex. The A1091P mutant retains the ability to bind XK at the plasma membrane but forms non-functional aggregates, whereas the M3080R mutant interacts inefficiently with XK, leading to little or no functional complex formation.

3.5. Giant cell morphology of I2763R-expressing cells

Western blot analysis showed that the expression level of the mouse VPS13A I2763R mutant protein was approximately 9.1% of that of wild-type VPS13A (Figure 4A). Accordingly, the cells expressing I2763R failed to respond to extracellular ATP with PtdSer exposure (Figure 4C), and no complex formation with XK was detected by BN-PAGE (Figure 4D). However, flow cytometry analysis showed that their FSC-A/SSC-A profiles were markedly different from those of *Vps13a*$^{-/-}$*DKO*-P2X7 cells or their transformants expressing wild-type VPS13A (Figure 5A). Specifically, both FSC-A and SSC-A were increased in I2763R-expressing cells, suggesting an increase in cell size and granularity. This phenotype was confirmed by microscopic observation of PlasMem-

stained cells, and quantitative image analysis demonstrated that I2763R-expressing cells were approximately 30% larger than *Vps13a*$^{-/-}$*DKO*-P2X7 cells or *Vps13a*$^{-/-}$*DKO*-P2X7 cells expressing wild-type VPS13A (Figure 5B).

Strikingly, giant-cell morphology was also observed when the I2763R mutant was expressed in wild-type WR19L cells containing endogenous VPS13A (Figure 5C), indicating a dominant phenotype of the mutant. Furthermore, the expression of I2763R in *Xk*$^{-/-}$*Xkrx*$^{-/-}$ cells still caused high FSC-A/SSC-A values (Figure 5C), suggesting that this phenotype is independent of XK/XKR2. Because cell size is linked to the growth rate and cell cycle progression (49, 50), I compared the growth kinetics. I2763R-expressing cells grew significantly slower [doubling time (T_d) = 14.63 h] than either parental *Vps13a*-null *DKO*-P2X7 [T_d = 12.10 h] or wild-type VPS13A-reconstituted cells [T_d = 11.73 h] (Figure 5D).

3.6. Damaged and fragmented ER in I2763R mutant

VPS13A is a lipid transfer protein that mediates lipid transfer between intracellular organelles and plasma membranes (21, 22). To determine which organelles were affected by the I2763R mutation, the cells were analyzed using transmission electron microscopy. As shown in Figure 6A, *Vps13a*-deficient cells displayed normal morphology (panel a), and re-expression of wild-type VPS13A had little effect (panel b), indicating that VPS13A is dispensable for maintaining plasma membrane and organelle integrity in *Vps13a*$^{-/-}$*DKO*-P2X7 cells. In contrast, cells expressing the I2763R mutant contained numerous vacuole-like structures (panel c), consistent with the increased SSC-A in the profile of flow cytometry (Figure 5A). Closer examination revealed that these vacuoles contained fragmented ER, and in some cases, they fused with the plasma membrane

(panels d, e). Swelling of the nuclear envelope was occasionally observed (panel c). Although mitochondria were largely intact, some showed signs of damage (panel e), whereas the Golgi apparatus appeared unaffected.

Fluorescent staining with ER-Tracker and ERseeing further confirmed these findings (Figure 6B). In *Vps13a*$^{-/-}$*DKO*-P2X7 cells and those expressing wild-type VPS13A, the ER was evenly distributed throughout the cytoplasm. In contrast, the I2763R mutant frequently caused polarized ER localization in plasma membrane protrusion. These regions often showed strong PlasMem staining, suggesting localized lipid enrichment (51). Together, these results demonstrate that the I2763R mutant disrupts ER integrity, leading to fragmentation and abnormal ER–plasma membrane interactions, possibly reflecting localized lipid transfer from the ER to the plasma membrane.

4. Discussion

In *Saccharomyces cerevisiae*, the single *VPS13* gene mediates the bulk lipid transfer required for the expansion and maintenance of organelle membranes (52, 53). In contrast, mammals possess four *VPS13* paralogs, and mutations in these genes are associated with distinct human disorders (42, 54-57): *VPS13A* mutations cause *VPS13A* disease (chorea-acanthocytosis); *VPS13B* mutations cause Cohen syndrome; *VPS13C* mutations have been linked to early onset of Parkinson's disease; and *VPS13D* mutations lead to early-childhood-onset ataxia-spasticity disorder.

Multiple deletions and missense mutations in *VPS13A*—generally regarded as recessive loss-of-function variants—have been identified in patients and are registered in the HGMD database (22). However, because of the lack of robust functional assays for VPS13A in mammalian cells, the biochemical defects underlying *VPS13A* disease remain poorly defined. Ryoden et al. (27) previously demonstrated that VPS13A is recruited to the plasma membrane via the membrane protein XK to form a complex that mediates ATP-stimulated PtdSer exposure. Using this assay system, I examined the functional consequences of a series of VPS13A deletions and missense mutations. The analysis of VPS13A C-terminal truncations, together with targeted XK mutagenesis, revealed that the β-hairpin of XK interacts with a protruding β–α–β structure motif within the C-terminal PH domain of VPS13A. Xu et al. (58) recently reported that *Vps13a*$^{-/-}$*Vps13c*$^{-/-}$ double-knockout mice, but not single-knockout mice, are embryonic lethal due to defective erythroid development, suggesting functional redundancy between VPS13A and VPS13C. Consistent with this idea, the C-terminal region of mouse VPS13C also carries a similar β–α–β fold (Figure S6). It would therefore be of interest to test whether

VPS13C can also form a complex with XK or XKR2 to support ATP-induced phospholipid scrambling.

In *S. cerevisiae*, *vps13a*-null mutations cause multiple phenotypes, including defective sporulation (59-61), loss of mitochondrial DNA (33), and impaired vacuolar protein sorting (62). Similarly, *Drosophila* carries a single *Vps13* gene, and its disruption leads to a reduced lifespan and age-dependent neurodegeneration (63). These phenotypes in yeast and fly mutants can be partially rescued by expression of human VPS13A (33, 59, 60, 63), indicating that VPS13 proteins in these organisms perform molecular functions similar to mammalian VPS13A. Notably, both yeast and *Drosophila* VPS13 proteins possess a C-terminal β–α–β motif (Figure S6), although XK homologs are absent in these organisms. It remains to be determined whether VPS13-interacting proteins in yeast or *Drosophila*, potentially searchable via the Molecular Interaction Search Tool (MIST, https://fgr.hms.harvard.edu/MIST), contain β-hairpin motifs analogous to that of XK.

Among the ten mouse VPS13A missense mutations analyzed in this study, six (L67P, I90K, A1091P, W2453R, I2763R, and M3080R) caused severe defects in protein expression and/or ATP-triggered PtdSer exposure (Table 1). In contrast, four mutants (S1446P, Q2689H, Y2713C, and R3084H) were expressed at appreciable levels and retained ATP-stimulated PtdSer exposure, suggesting only modest effects on expression and/or scramblase activity. Notably, three of the residues showed modest phenotypes (including Q2689, identified in a schizophrenia patient) are not conserved in VPS13C, whereas all six essential residues associated with severe functional impairment are highly conserved (Figure S7), underscoring their critical roles in protein stability and function.

L67, I90, and W2453 are located within β-strands of mouse VPS13A (Figure 7). The L67P mutation introduces a proline residue that is predicted to disrupt β-strand integrity, whereas I90K and W2453R mutations introduce basic residues into hydrophobic cores (I90 surrounded by L48, F55, L88, I160 and Y162; W2453 surrounded by V2462, I2472, L2481, and F2494) (Figure S8), thereby abolishing hydrophobic interactions and folding stability. Among the remaining nonfunctional variants, M3080R likely disrupts the β–α–β structure essential for XK binding, while A1091P, located in the central region of the protein, may obstruct the phospholipid passage through the VPS13A channel. Collectively, these results support the idea that *VPS13A* disease can arise from mutations that impair VPS13A-mediated ATP-dependent PtdSer exposure.

Based on these findings, I propose the following model: ATP released from neuronal tissues, particularly under injury conditions, activates P2X7 receptors that are highly expressed in microglia and oligodendrocytes (64). P2X7 activation promotes inflammatory signaling via the NF-κB pathway (16) and simultaneously induces PtdSer exposure through activation of the VPS13A–XK complex (27). Because PtdSer on the cell surface exerts anti-inflammatory effects (65), dysfunction of the VPS13A system may lead to chronic neuroinflammation and progressive neuronal loss (66).

The I2763R mutant, despite reduced expression and loss of ATP-stimulated PtdSer exposure, exhibited a strong dominant effect on cell size. Interestingly, *S. cerevisiae* VPS13 D716H and L1627S alleles are dominant gain-of-function mutations that bypass the ER–mitochondrial contact system (67). Likewise, the mouse VPS13A I2763R mutation may bypass the ER–plasma membrane contact system, promoting excessive lipid transfer and plasma membrane expansion, as observed in osmotically induced membrane growth (68). The presence of damaged nuclear and mitochondrial membranes

in I2763R-expressing cells is consistent with VPS13A's proposed role in lipid transfer between the ER and multiple organelles (21). It will be important to test whether the corresponding yeast mutant (I2749R) (60) exhibits similar phenotypes. Moreover, as the yeast D716 and L1627 residues are well conserved in mouse and human VPS13A, it would be worthwhile to determine whether equivalent mouse mutations also exert dominant effects on lipid transfer between the ER and mitochondria.

5. Materials and methods

5.1. Cell lines, antibodies, and reagents

WR19L is a mouse T-cell lymphoma cell line (ATCC: TIB-52). *Tmem16f*$^{-/-}$*P2rx7*$^{-/-}$ WR19L (*DKO*) and *Vps13a*$^{-/-}$*DKO*, as well as their transformants expressing mouse P2X7 and/or VPS13A (*DKO*-P2X7, *Vps13a*$^{-/-}$*DKO*-P2X7, and *Vps13a*$^{-/-}$*DKO*-P2X7-VPS13A) were described previously (27). WR19L and its derivatives were grown in RPMI1640 supplemented with 10% FBS. *DKO*-P2X7 and *Vps13a*$^{-/-}$*DKO*-P2X7 cells were grown in the presence of 800 μg/ml G418, whereas *Vps13a*$^{-/-}$*DKO*-P2X7-VPS13A and all other *Vps13a*$^{-/-}$*DKO* transformants expressing VPS13A variants were grown in the presence of 800 μg/ml G418 and 1 μg/ml puromycin. HEK293T cells (ATCC: CRL-3216) were cultured in DMEM supplemented with 10% FBS.

Rabbit anti-XK (#HPA019036) and anti-VPS13A (#HPA021662) Abs were purchased from Atlas Antibodies. Horseradish peroxidase (HRP)-rabbit anti-GFP (anti-GFP pAb-HRP-DirecT) (#598-7) and HRP-goat anti-rabbit immunoglobulins (IgGs) (#P0448) were from MBL and Agilent, respectively. Alexa 647- (#MCA4713A647) or Alexa 488- (#MCA4713A488) conjugated rat anti-mouse P2X7 mAbs (clone Hano43) were purchased from Bio-Rad Laboratories. Cy5-Annexin V (#AB_2869267) was from BD Biosciences.

Hoechst 33342 (#H3570), ER-Tracker Blue-White DPX (#HY-D1429), and SYTOX Blue (#S34857) were obtained from ThermoFisher Scientific. PlasMem Bright Red (51), ERseeing (Endoplasmic Reticulum Green) (69), propidium iodide (PI), and colloidal gold protein stain were purchased from Dojindo (#346-09771), Funakoshi (#FDV-0038), Sigma-Aldrich (#P4170), and Bio-Rad Laboratories (#1706527), respectively. (*p*-Amidinophenyl)Methanesulfonyl fluoride Hydrochloride (*p*-APMSF)

was obtained from Wako (#019-26331). Pefabloc SC (#1142986800) and cOmplete EDTA-free protease inhibitor cocktail (#11873580001) were obtained from Roche. Tris(2-carboxyethyl)phosphine hydrochloride (TCEP-HCl) was obtained from Nacalai Tesque (#07277). *n*-Dodecyl-β-D-maltoside (DDM) and cholesteryl hemisuccinate (CHS) were from Dojindo (#341-06161) and Sigma-Aldrich (#C6512), respectively. FuGENE 6 was purchased from Promega (#E2691).

5.2. Plasmids

pGag-pol-IRES-bsr (70) was a gift from T. Kitamura. pCMV-VSV-G and pAdVAntage were obtained from RIKEN (#RDB04392) and Promega (#U47294), respectively. The human (h)VPS13A^mCherry plasmid (53) was obtained from Addgene (#118758), and its coding sequence was transferred to pPEF-BOS-EX (RIKEN RDB18971) to generate pPEF-hVPS13A^mCherry. The expression vectors for mouse (m)P2X7 (71) and pPEF-mVPS13A (27) were described previously. The GFP portion of pMXs-puro-mXK-GFP and pMXs-puro-mXKR2-GFP (40) was replaced with monomeric enhanced GFP (mEGFP) (72). Mutant VPS13A and XK were constructed using pPEF-mVPS13A (Figure S5) and pMXs-puro-mXK-mEGFP as templates, and the constructs were verified by DNA sequencing. The forward and reverse primers used for PCR are listed in Tables S2 and S3 and were synthesized by FASMAC Co., Ltd.

To delete mCherry from pPEF-hVPS13A^mCherry, two DNA fragments were prepared by PCR, one with a forward primer containing BlpI and a reverse joint primer, and the other with a forward joint primer and a reverse primer containing SwaI (Table S1). The PCR products were purified using the ExoSAP-IT Express PCR Product Cleanup Kit (ThermoFisher Scientific, #75001) and inserted between the BlpI-SwaI sites

of pPEF-hVPS13A^mCherry using the In-Fusion HD Cloning Kit (TaKaRa, #639650) to generate pPEF-hVPS13A. The resulting plasmids were transformed into *E. coli* DH5α or XL10-Gold cells (Agilent Technologies, #200314).

For the L67P and I90K mutants of mouse VPS13A, two DNA fragments were generated by PCR using Primer F1 and L67P_R or I90K_R, and L67P_F or I90K_F with Primer R1, respectively (Table S2 and Figure S5). The PCR products were inserted between the PacI and EcoRV sites of pPEF-mVPS13A. The other mutants were prepared similarly with mutagenesis primers along with the corresponding forward and reverse primers. For R3127Δ, two DNA fragments were generated by PCR using Primer_F6 and R3127Δ_R, and R3127Δ_F and Primer_R6, whereas for E3136Δ, Primer_F6 and E3136Δ_R, and E3136Δ_F and Primer_R6 were used. The resulting fragments were inserted into NheI-digested pPEF-mVPS13A vector.

For mouse XK mutants, two PCR fragments were prepared with Primer_F7 and reverse mutagenesis primer, and forward mutagenesis primer and Primer_R7 (Table S3) and inserted between BamHI and EcoRI of pMXs-puro-mXK-mEGFP.

5.3. Cell transformation

To introduce the VPS13A expression plasmid into WR19L-derived cell lines, DNA (10–20 μg) was digested with PvuI and electroporated into 1×10^6 cells using a NEPA21 Super Electroporator (Nepa Gene). After 48 h, puromycin was added to the culture medium at a final concentration of 1.0 μg/ml, cultured for 2–10 days, and subjected to limiting dilution. At least 10 puromycin-resistant clones were screened for VPS13A expression by western blotting, and one high-expressing clone was selected for further analyses.

Regarding the transformation of mouse P2X7, XK, XKR2, or their derivatives, HEK293T cells were transfected with pMXs-puro or pMXs-neo vectors carrying the respective cDNA, along with pGag-pol-IRES-bsr, pCMV-VSV-G, and pAdVAntage using FuGENE 6, and cultured for 48 h. Retroviruses in the supernatant were collected by centrifugation at 6,000 × *g* for 16 h at 4 °C and used to infect WR19L derivatives. At 24 h later, puromycin or G418 was added to a final concentration of 1.0 μg/ml or 800 μg/ml, respectively, and P2X7- and/or GFP-positive transformants were sorted using FACSAriaII (BD Bioscience).

5.4. Gene editing

Mouse *Xk* and *Xkrx* genes were knocked out using the CRISPR/Cas9 system (73), as described previously (27). The target sequence for sgRNA for *Xk* (5'-CTTTCTCCACCTCCTCTGAA-3') was from Ryoden et al. (27), while the mouse sequence (5'-TGTAGTCATCATACTTGATC-3') corresponding to that used to knock out human *XKRX* (30) was adapted for the *Xkrx* gene. Complementary oligonucleotides carrying the sgRNA sequence were annealed, ligated into pX459v2 (74), and introduced into WR19L cells twice by electroporation at 3–10-day interval, subjected to limiting dilutions, and screened by sequencing the target regions of the *Xk* and/or *Xkrx* genes.

5.5. Preparation of whole-cell lysates and membrane fractions

To prepare whole-cell lysates, 1.5×10^6 cells were incubated at 4 °C for 1 h in 0.1 ml of lysis buffer [20 mM Tris-HCl (pH 7.5), 50 mM KCl, 1 mM $MgCl_2$, 10% glycerol, 1% DDM, 0.1% CHS, 1 mM *p*-APMSF, and a protease inhibitor mixture (cOmplete, EDTA-free)]. After centrifugation at 20,000 × *g* and 4 °C for 15 min, the supernatants

were collected as whole-cell lysates. Protein concentration was determined using the Pierce BCA Protein Assay Kit (ThermoFisher Scientific, #23225).

For the membrane fractions, 1.6–2.0 × 10^7 cells in 4 ml of 20 mM HEPES-NaOH buffer (pH 7.0) containing 150 mM NaCl, 1 mM EDTA, 1 mM EGTA, 0.4 mM Pefabloc SC, 1 mM *p*-APMSF, 1 mM TCEP, and a protease inhibitor mixture were disrupted at 4 °C using an ultrasonic disrupter (QSONICA) (0.5-s sonication at an amplitude of 30 followed by 0.5-s cooling intervals for a total sonication period of 1 min). After successive centrifugation at 800 × *g* at 4 °C for 10 min and at 8,000 × *g* for 10 min, membrane fractions were collected by centrifugation at 100,000 × *g* for 1 h, resuspended in 0.09 mL of lysis buffer, homogenized with 29G needle syringes for 10–25 strokes, and incubated at 4 °C for 2 h. Insoluble materials were removed as described above, and the supernatant was used as the membrane fraction.

5.6. SDS-PAGE, BN-PAGE, and western blotting

For SDS-PAGE, whole-cell lysates (4.7 μg) or membrane fractions (1.1 μg) were incubated at room temperature for 15 min to 2 h in SDS sample buffer [62.5 mM Tris-HCl (pH 6.8), 2% SDS, 10% glycerol, 2.5% 2-mercaptoethanol, and 0.005% bromophenol blue] and separated on either a 7.5% SDS-PAGE gel or a 5–10% gradient gel. HiMark Pre-stained Protein Standard (ThermoFisher Scientific, #LC5699) and Precision Plus Protein Standards, Dual Color (Bio-Rad Laboratories, #1610374) were used as molecular weight markers.

BN-PAGE was performed using a system provided by ThermoFisher Scientific. In brief, membrane fractions (1.1 μg) were mixed with 1/4 volume of NativePAGE Sample Buffer (#BN2003) and 1/20 volume of NativePAGE 5% G-250 Sample Additive

(#BN2004), and loaded onto a NativePAGE 4–16% Bis-Tris gel (#BN2111BX10 or #BN2112BX10). Electrophoresis was performed at 150 V at 4 °C for 35 min, after which the concentration of CBB G-250 in the running buffer was reduced from 0.02% to 0.002%. Electrophoresis was then performed sequentially at 150 V for 25 min, 250 V for 30 min, and 350 V for 20 min. NativeMark Unstained Protein Standard (#LC0725) was used as the molecular weight marker.

For western blotting, proteins were transferred from gels to polyvinylidene difluoride (PVDF) membranes (Immobilon-P, Merck, #IPVH00010) either immediately after SDS-PAGE or after BN-PAGE gels were incubated in SDS-PAGE running buffer [25 mM Tris-HCl (pH 8.3), 192 mM glycine, 0.1% SDS] at room temperature for 15 min. Membranes were blocked with 5% skim milk and probed with HRP-conjugated Abs. Signals were detected using the Immobilon Western Chemiluminescent HRP substrate (Merck, #WBKLS0500). As a loading control, proteins on the membranes were visualized by staining with CBB R-250 or Colloidal Gold Protein Stain.

5.7. Flow cytometry and ATP-induced PtdSer exposure

ATP-induced exposure of PtdSer was assayed by Annexin V binding, as described previously (71). Briefly, the cells were seeded at a density of 2×10^5 cells/ml one day before the experiment. On the day of analysis, 4×10^5 cells were washed with chilled PBS and pre-incubated for 10 min at 4 °C in 400 µl of annexin buffer [10 mM HEPES-NaOH (pH 7.5), 140 mM NaCl, and 2.5 mM $CaCl_2$] containing Cy5–Annexin V (1:1000 dilution) and either 2.5 µg/ml PI or 250 nM SYTOX Blue. The cells were then stimulated with 500 µM ATP at 4 °C for 10 min. Annexin V–binding profiles were acquired by flow

cytometry using a FACSCanto II (BD Biosciences) and analyzed with FlowJo software (Ver. 7.6.5; BD Biosciences).

5.8. Confocal microscopy and cell size estimation

To localize XK and XKR2, 2×10^5 cells expressing XK–mEGFP or XKR2–mEGFP were washed with PBS and suspended in 0.2 ml of HBSS supplemented with 5 μg/ml Hoechst 33342. The cells were placed in a glass-bottom dish (Matsunami, #D141400) and observed using a confocal fluorescence microscope (Evident, FV1000-D IX81). To assess ER morphology, cells were incubated at 37 °C for 15 min with 100 nM ER-Tracker Blue-White DPX or ERseeing, collected by centrifugation, resuspended in HBSS, and observed using a confocal microscope, as described above. In some cases, PlasMem Bright Red (1:100 dilution) was added to the staining solution to localize plasma membranes.

To assess cell size, cells were incubated at 37 °C for 5 min with 5 μg/ml Hoechst 33342 and PlasMem Bright Red (1:100 dilution) in HBSS. After centrifugation, the cells were resuspended in HBSS and observed under a confocal fluorescence microscope. Fluorescent images were recognized using Cellpose-SAM for automatic segmentation and labelling of the region of interest (ROI) (75). ROI corresponding to incorrectly segmented or edge-captured cells were manually excluded from the analysis. The area of each ROI was measured using Fiji (Image J2, version 2.16.0/1.54p).

5.9. Electron microscopy

Cells (1×10^6) were fixed overnight at 4 °C in 0.1 ml of 0.1 M phosphate buffer (pH 7.4) containing 2.5% glutaraldehyde and 2% paraformaldehyde. The samples were post-fixed with 2% osmium tetroxide (OsO_4) for 1 h and block-stained with 2% aqueous uranyl

acetate. Following dehydration through a graded ethanol series, the samples were embedded in Epon 812 resin (TAAB Epon 812; EM Japan, #342). The sections were cut to a thickness of 70-80 nm using a UC6 ultramicrotome (Leica, Ultracut CUT N), stained with lead citrate and uranyl acetate, and examined using a JEM-1400Flash transmission electron microscope (JEOL).

5.10. AlphaFold-based predictions

Structural models of XKR and VPS13 family members were generated using the AlphaFold 3 online server (https://alphafoldserver.com) (32). For the VPS13A–XK complex, the full-length amino acid sequence of mouse VPS13A (NP_766616.2) was modeled in combination with that of mouse XK (NP_075989.1). Each AlphaFold prediction provided the five highest-ranked models, from which the top-ranked structure was selected for further analyses. Molecular graphics and analyses were performed using UCSF ChimeraX (version 1.10), developed by the Resource for Biocomputing, Visualization and Informatics at the University of California, San Francisco (76).

5.11. Statistics

Statistical analysis was performed with GraphPad Prism (version 10.5.0). The significance of the differences was calculated using one-way or two-way ANOVA with Dunnett's, Tukey's, or Šídák's multiple comparison test. Differences were considered significant when the *P*-value was less than 0.05.

6. Figures

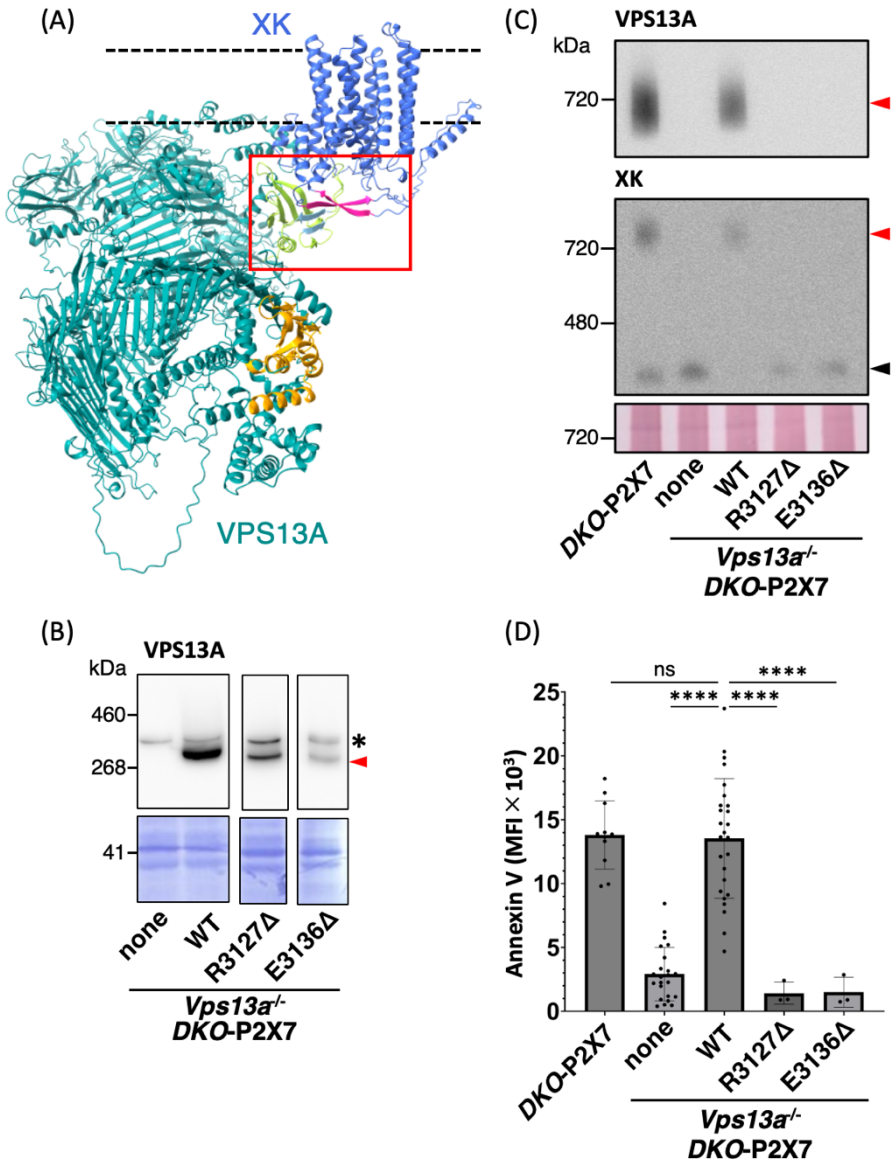

Figure 1. Requirement of the C-terminal domain of VPS13A for ATP-induced PtdSer exposure

(legend on next page)

(**A**) AlphaFold 3-predicted VPS13A–XK structure. The structure of the mouse VPS13A–XK complex was predicted using AlphaFold 3 (https://www.alphafoldserver.com) (32) with ipTM = 0.72 and pTM = 0.54. VPS13A is shown in dark cyan and XK in royal blue. The N-terminal chorein and the C-terminal PH domains of VPS13A are highlighted in orange and yellow-green, respectively. The β-hairpin of XK is shown in pink, and the two β-strands in the PH domain of VPS13A are shown in light blue. The dotted lines indicate the predicted membrane bilayers. (**B–D**) Effect of VPS13A C-terminal deletion mutants on their interaction with XK and ATP-induced PtdSer exposure. Wild-type (WT), R3127Δ, and E3136Δ VPS13A were stably expressed in *Vps13a*$^{-/-}$*DKO*-P2X7 cells. (**B**) Whole-cell lysates were separated by SDS-PAGE and analyzed by western blotting using anti-VPS13A Ab. Red arrowhead, VPS13A; *, non-specific band. (**C**) Membrane fractions from *DKO*-P2X7, *Vps13a*$^{-/-}$*DKO*-P2X7, and their transformants expressing none, WT, R3127Δ, or E3136Δ mouse VPS13A were separated by BN-PAGE and analyzed by western blotting with anti-VPS13A (upper) or anti-XK (lower) Abs. Red arrowheads indicate the VPS13A–XK complex, and the black arrowhead indicates XK. (**D**) *DKO*-P2X7, *Vps13a*$^{-/-}$*DKO*-P2X7, and their transformants expressing none, WT, R3127Δ, or E3136Δ mouse VPS13A were treated with ATP. PtdSer exposure was assessed by flow cytometry using Cy5–Annexin V, and expressed as MFI. Data are presented as mean ± SD (bars) of at least three independent experiments. The membranes for western blotting were stained with CBB (**B**) or Colloidal Gold Protein Stain (**C**). Statistical significance was determined using one-way ANOVA with Dunnett's multiple comparison test (ns, not significant; ****$P < 0.0001$).

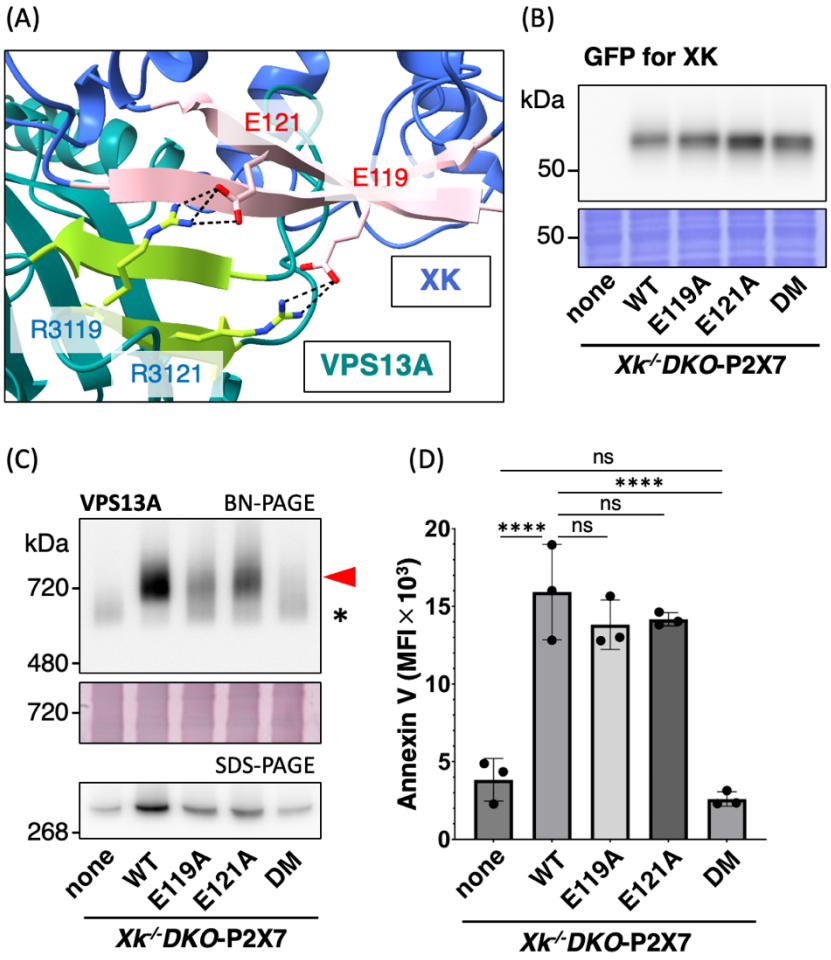

Figure 2. Interaction between mouse VPS13A and XK

(legend on next page)

(**A**) Residues mediating the VPS13A–XK interaction. The red boxed region in Figure 1A is shown enlarged. Hydrogen bonds are formed between XK β-hairpin residues E119/E121 and VPS13A C-terminal β-sheet residues R3121/R3119. (**B–D**) Effects of XK mutations on VPS13A binding and scramblase activity. *Xk*$^{-/-}$*DKO*-P2X7 cells were transformed with WT, E119A, E121A, or E119A/E121A double mutant (DM) XK. (**B**) Whole-cell lysates were analyzed by SDS-PAGE and immunoblotting with anti-GFP Ab. (**C**) Membrane fractions were analyzed by BN-PAGE (upper panels) and SDS-PAGE (lower panel), and immunoblotted with anti-VPS13A Ab. Arrowheads indicate the VPS13A–XK complex, and the asterisk marks an unidentified protein. (**D**) Cells were stimulated with ATP, and PtdSer exposure was analyzed by flow cytometry using Cy5–Annexin V. Data are presented as mean ± SD (bar) of three independent experiments. The membranes for western blotting were stained with CBB (**B**) or Colloidal Gold Protein Stain (**C**). Statistical significance was determined using one-way ANOVA with Dunnett's multiple comparison test (ns, not significant; ****$P < 0.0001$).

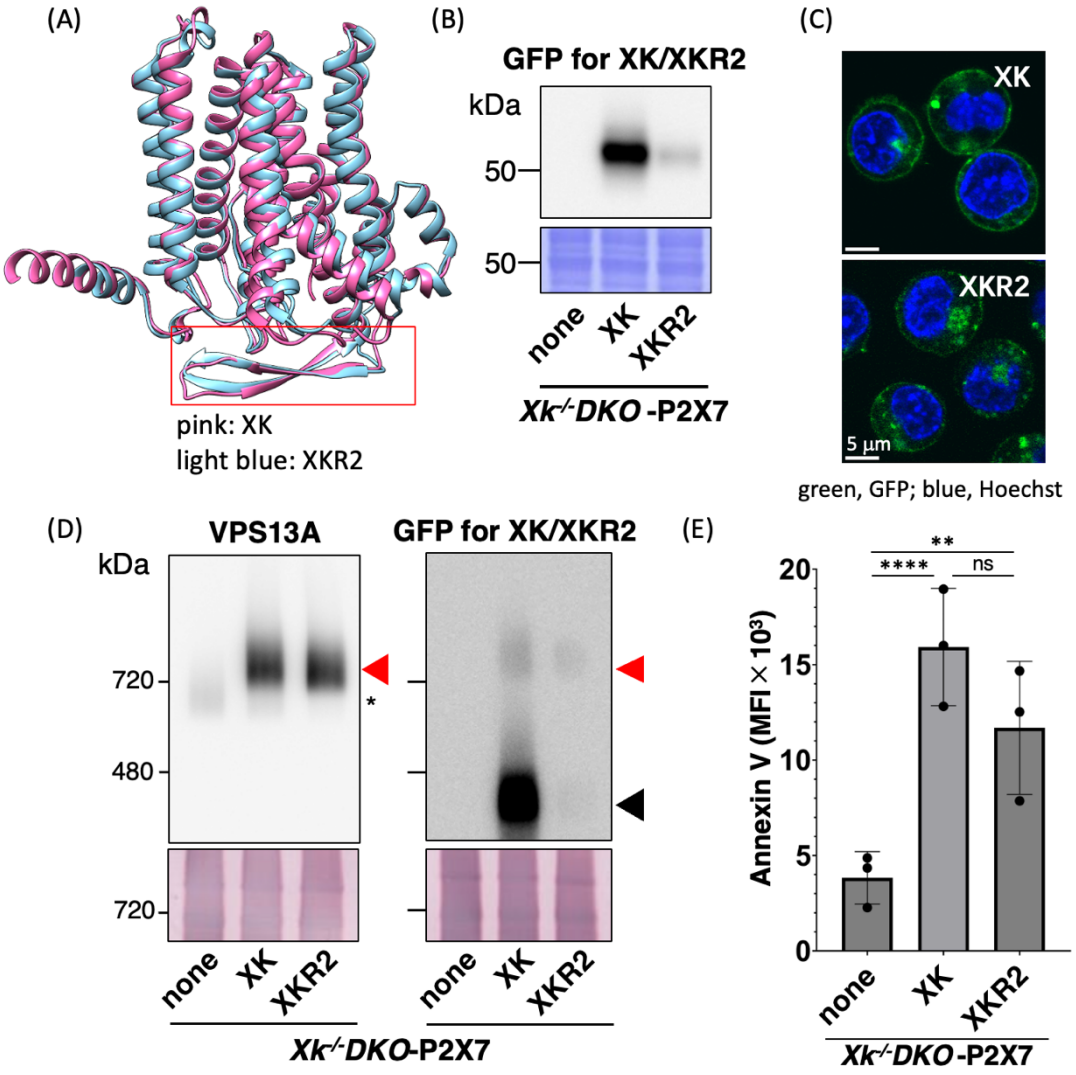

Figure 3. Interaction of XKR2 with VPS13A and its ability to support ATP-induced PtdSer exposure

(legend on next page)

(**A**) Structural comparison of XK and XKR2. AlphaFold 3-predicted structures of mouse XK (AlphafoldDB, Q9QXY7) and XKR2 (AlphafoldDB, Q5GH68), excluding their N- and C-terminal regions, are shown. The β-hairpin region is enclosed in a red box. (**B–E**) Functional analysis of XKR2. *Xk*$^{-/-}$*DKO*-P2X7 cells were transfected with mEGFP-tagged mouse XK or XKR2. (**B**) Whole-cell lysates were analyzed by SDS-PAGE and immunoblotting with an anti-GFP Ab (top panel) or stained with CBB (bottom panel). (**C**) GFP fluorescence was observed using a microscope. (**D**) Membrane fractions were analyzed by BN-PAGE and immunoblotting with anti-VPS13A or anti-GFP Abs or stained with Colloidal Gold Protein Stain. Red arrowhead, VPS13A–XK–mEGFP or XKR2–mEGFP complex; band marked with an asterisk is an unidentified protein; black arrowhead, uncomplexed XK. (**E**) Cells were treated with ATP and analyzed by flow cytometry for PtdSer exposure, and expressed as MFI. Data are presented as the mean ± SD (bar) of three independent experiments. Statistical significance was determined using Dunnett's multiple comparison test (ns, not significant; ***$P < 0.001$; ****$P < 0.0001$).

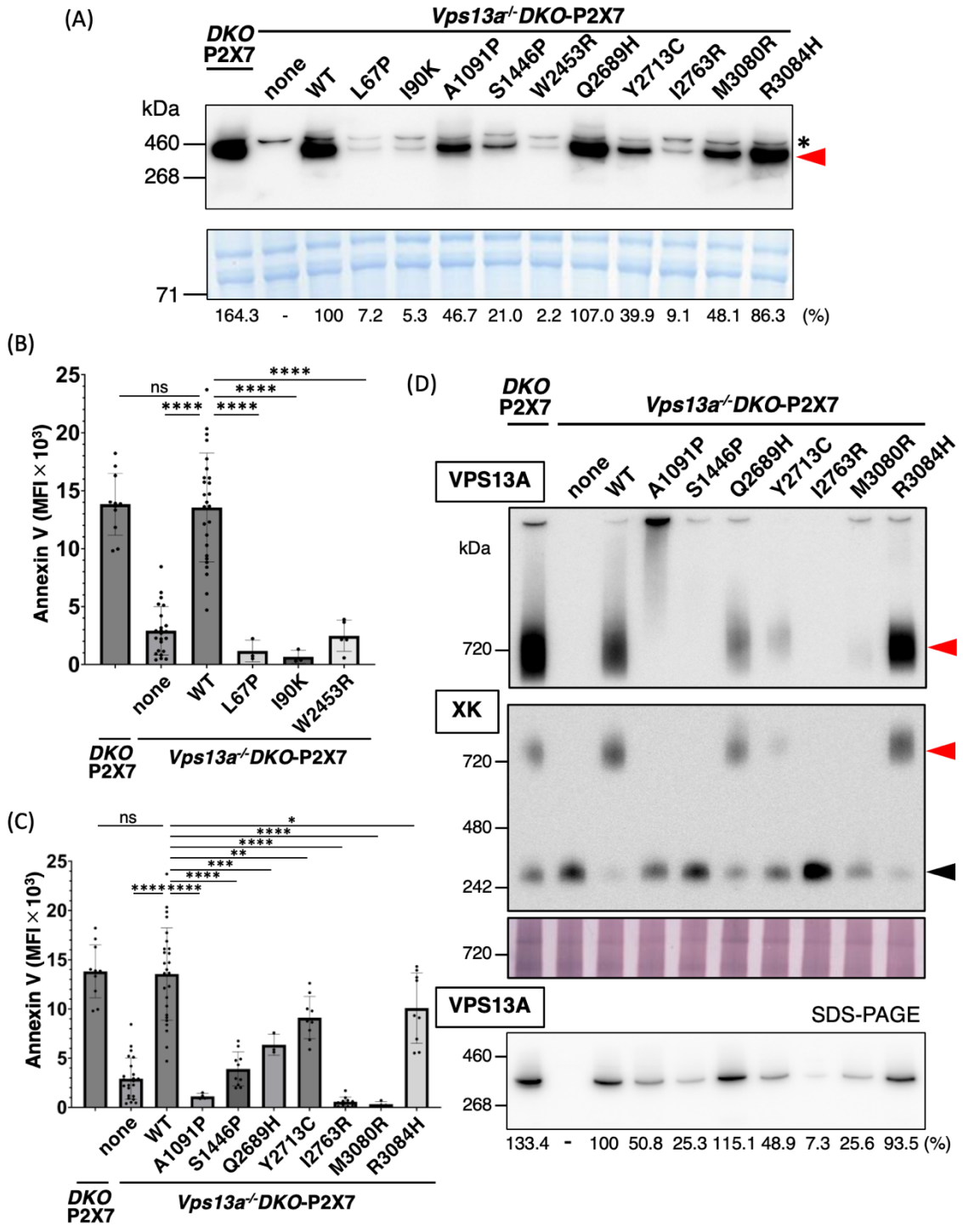

Figure 4. Characterization of VPS13A missense mutations

(legend on next page)

(**A**) Stable expression of VPS13A missense mutations. *Vps13a*$^{-/-}$*DKO*-P2X7 cells were stably transformed with WT or the indicated mouse VPS13A mutants. Whole-cell lysates from *DKO*-P2X7, *Vps13a*$^{-/-}$*DKO*-P2X7 (none), and mutant transformants were analyzed by SDS-PAGE and western blotting using anti-VPS13A Ab. The CBB-stained membrane is shown below. Red arrowhead, VPS13A; *, non-specific band. (**B** and **C**) ATP-induced PtdSer exposure. Transformants expressing WT or mutant mouse VPS13A were treated with ATP, stained with Cy5–Annexin V, analyzed by flow cytometry, and expressed as MFI. Data are presented as mean ± SD (bar) of more than three independent experiments. Statistical significance was determined using Dunnett's multiple comparison test (ns, not significant; *$P < 0.05$; **$P < 0.01$; ***$P < 0.001$; ****$P < 0.0001$). (**D**) Complex formation with XK. Membrane fractions were analyzed by BN-PAGE (upper panel) and SDS-PAGE (bottom panel), and western blotting with anti-VPS13A or anti-XK Abs. Red arrowheads indicate the VPS13A–XK complex, and black arrowhead indicates free XK. Membranes were stained with CBB (**A**) or Colloidal Gold Protein Stain (**D**). In (**A**) and (**D**), the band intensity detected by western blotting was quantified by densitometry and expressed relative to that detected in cells expressing WT-VPS13A.

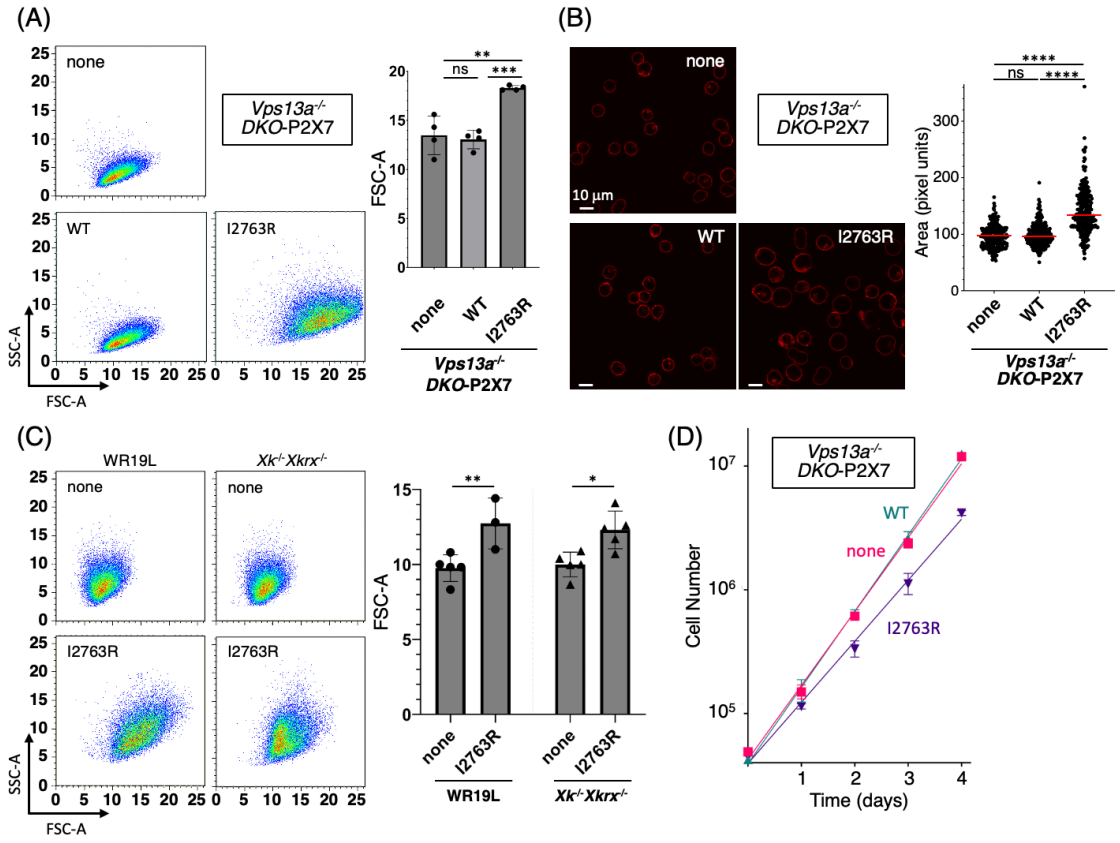

Figure 5. Characterization of VPS13A I2763R mutant

(**A**) Flow cytometry analysis. *Vps13a*$^{-/-}$*DKO*-P2X7 and its transformants expressing WT or I2763R mouse VPS13A were analyzed by flow cytometry. FSC-A/SSC-A profiles of the PI-negative population are shown. The experiments were independently performed for three times, and the FSC-A values are presented as mean ± SD (bar). (**B**) Microscopy-based size measurements. The cells were stained with PlasMem and observed using a confocal microscope. Cell size was quantified using Cellpose-SAM and Fiji; the distributions (in pixel units) are shown as scatter plots. (**C**) Effect of I2763R in the *Xk/Xkrx*-null genetic background. I2763R mouse VPS13A was expressed in WR19L or *Xk*$^{-/-}$*Xkrx*$^{-/-}$WR19L cells, and stable transformants were analyzed for FSC-A/SSC-A profiles using flow cytometry. Mean ± SD (bar) of three independent experiments is shown. (**D**) Growth assay. Cells were seeded at 4 × 10^4 cells/ml and cultured for 4 days. The growth was monitored over time. Statistical significance in (**A**) and (**B**) was determined using one-way ANOVA with Dunnett's multiple comparison test, while in (**C**) was determined using two-way ANOVA with Šídák's multiple comparison test. ns, not significant; *$P < 0.05$; **$P < 0.01$; ***$P < 0.001$; ****$P < 0.0001$.

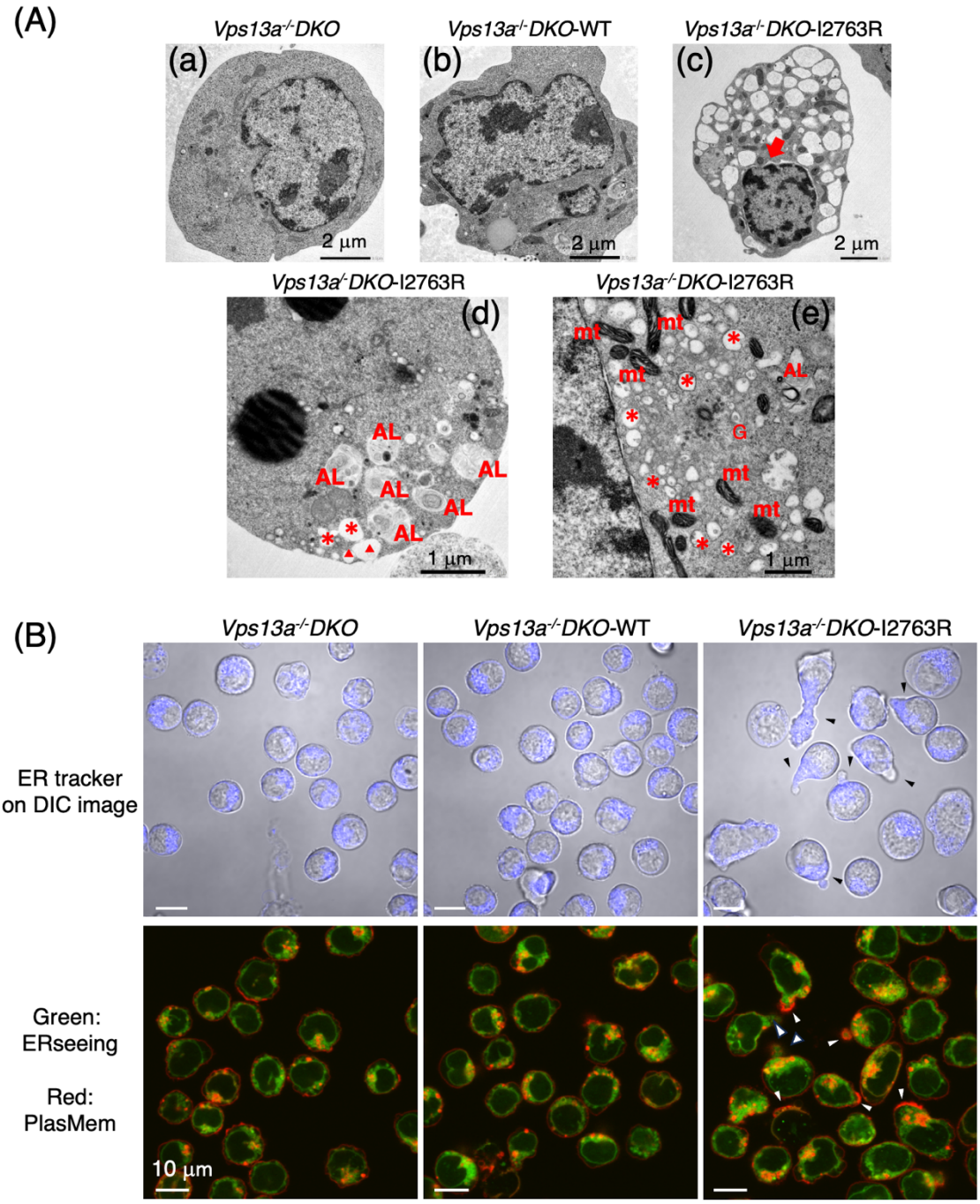

Figure 6. Damaged ER in cells expressing the I2763R VPS13A mutant

(legend on next page)

(**A**) Transmission electron microscopy. mt, mitochondria; G, Golgi apparatus; AL, autophagosome/lysosome; *, fragmented or damaged ER; red triangles, damaged ER fusing with plasma membrane. The swollen nuclear membrane is indicated by a red arrow. (**B**) Confocal microscopy images. Cells were stained with ER-Tracker (top panels) or ERseeing and PlasMem (bottom panels). The regions where ERs are polarized to the plasma membrane are indicated by arrowheads.

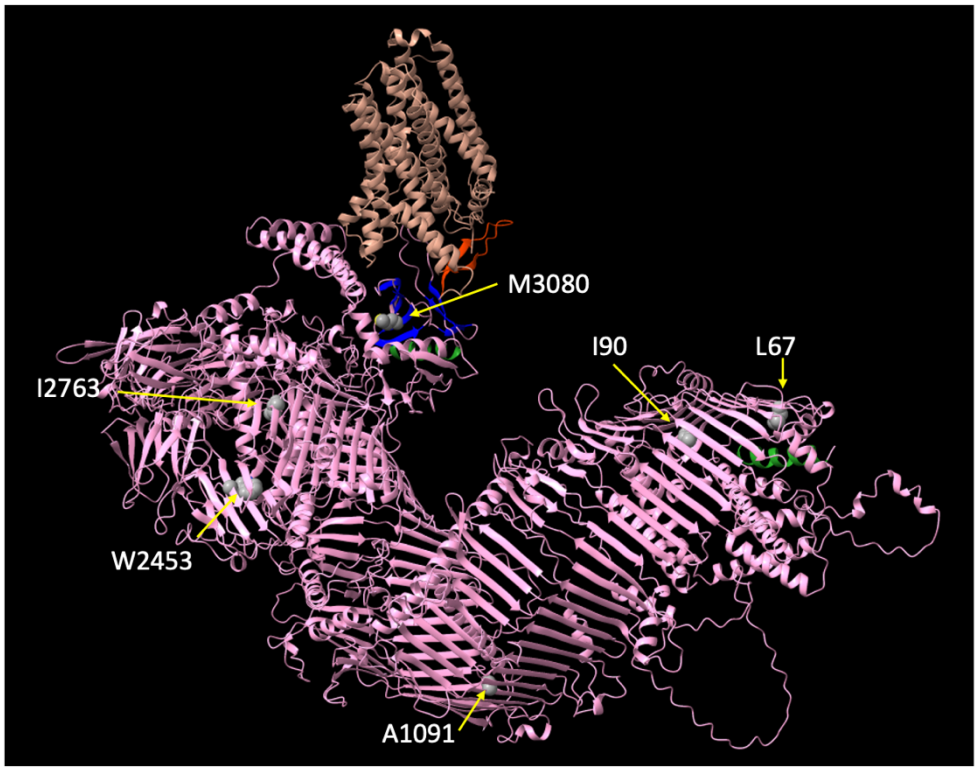

Figure 7. Pathological missense mutations in the mouse VPS13A

The AlphaFold 3-predicted tertiary structure of the mouse VPS13A–XK complex is shown with six residues, the missense mutation of which has a strong impact on protein expression or function. XK is shown in tan, with the hairpin structure in orange. VPS13A is colored magenta, where the β-strands and α-helix in the N- and C-termini are blue and green, respectively. The essential 6 residues are shown as ball-and-string or sphere structures with colored elements.

7. Tables

Table 1. Summary of mouse VPS13A mutants harboring the corresponding human mutations

Patients			Biochemical properties of mouse mutants					
Human mutant	**Refs**	**Disease**	**Mouse mutant**	**Protein expression[1]**	**Membrane fraction[2]**	**Complex with XK**	**PtdSer-exposure[3]**	**Comment[4]**
L67P	(45)	*VPS13A* disease	<u>L67P</u>	7.2	n.e.	n.e.	No	(I) Expression defect
I90K	(42)	*VPS13A* disease	<u>I90K</u>	5.3	n.e.	n.e.	No	(I) Expression defect
A1095P	(38)	*VPS13A* disease	**A1091P**	46.7	50.8 (1.09)	No	No	(II) Functional defect
S1452P	(42)	*VPS13A* disease	S1446P	21.0	25.3 (1.20)	No	23.1 (1.1)	(III) Moderate effect on expression
W2460R	(38)	*VPS13A* disease	<u>W2453R</u>	2.2	n.e.	n.e.	No	(I) Expression defect
Q2697H	(47)	schizophrenia	Q2689H	107	115.1 (1.08)	Yes	36.9 (0.35)	(III) Moderate effect on the function
Y2721C	(42)	*VPS13A* disease	Y2713C	39.9	48.9 (1.23)	Yes	48.6 (1.22)	(III) Moderate effect on expression
I2771R	(43)	*VPS13A* disease	**<u>I2763R</u>**	9.1	7.3 (0.80)	No	No	(IV) Adverse dominant effect
M3088R	(46)	*VPS13A* disease	**M3080R**	48.1	25.6 (0.53)	No	No	(II) Functional defect
R3092H	(44)	*VPS13A* disease	R3084H	86.3	93.5 (1.08)	Yes	60.6 (0.65)	(III) Moderate effect on the function

[*1] The expression level of each mouse mutants was relative to that of wild-type VPS13A, as determined by immunoblotting of total cell lysates (Figure 4A). Mutants expressed at <10% of wild-type were regarded as "Expression defect", and no further biochemical analysis was performed (n.e., not examined), except for I2763R.

[*2] VPS13A protein levels in the membrane fraction (Figure 4D) were expressed relative to those of wild-type VPS13A. Values in parentheses indicates normalization to total expression.

[*3] The activity of each mouse mutant in ATP-stimulated P2X7-mediated PtdSer exposure was evaluated relative to that of wild-type VPS13A protein. Mutants with activity below non-transformed *Vps13a*$^{-/-}$*DKO*-P2X7 cells are marked as "No". Parenthesis indicate activity normalized to total expression.

[*4] Mutations were categorized into four groups: (I) expression defect, (II) functional defect, (III) moderate effect on either expression or function, and (IV) adverse dominant effect. Types (I), (II), and (IV) are indicated by underlining, boldface, and bold underlining, respectively.

8. Supplementary Figures

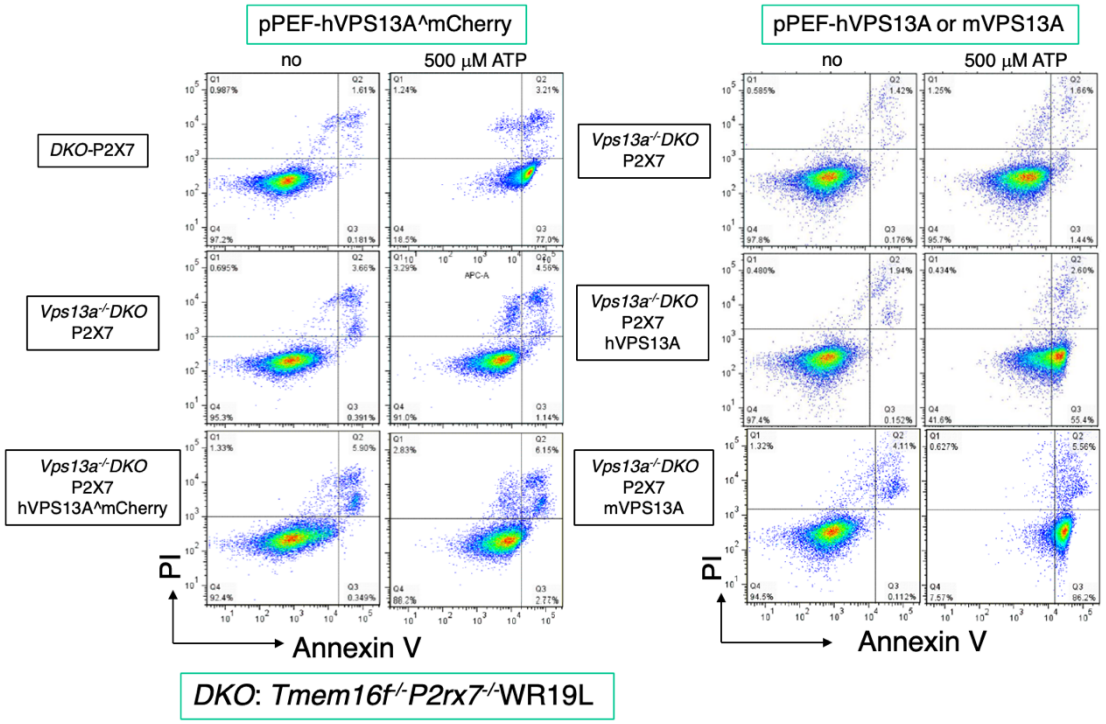

Figure S1. Comparison of the activity of internally mCherry-tagged VPS13A and intact VPS13A in supporting ATP-stimulated P2X7-mediated PtdSer exposure

Expression plasmids (pPEF-hVPS13A^mCherry, pPEF-hVPS13A, and pPEF-mVPS13A) were introduced into *Vps13a*$^{-/-}$*DKO*-P2X7 cells by electroporation, and stable transformants were established by culturing the cells in the presence of puromycin. *DKO*-P2X7, *Vps13a*$^{-/-}$*DKO*-P2X7, and transformants expressing hVPS13A^mCherry (left panels), hVPS13A, or mVPS13A (right panels) were incubated at 4 °C with or without ATP for 5 min, stained with Cy5-Annexin and PI, and analyzed by flow cytometry.

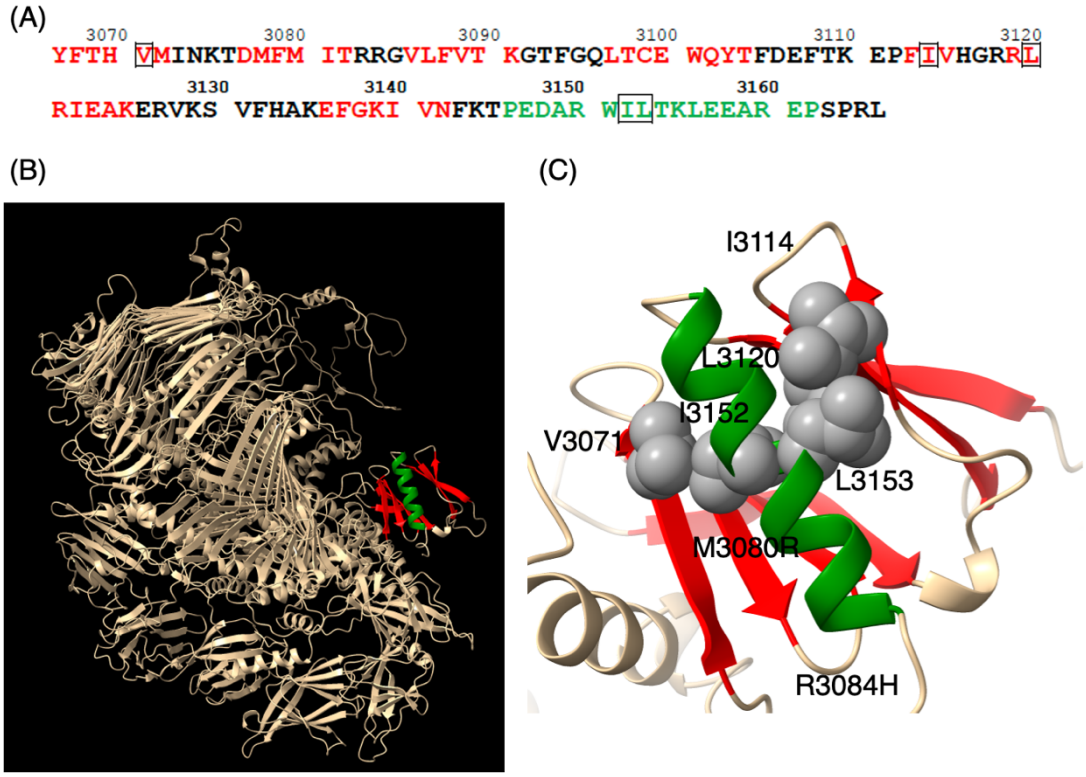

Figure S2. Knob-like structure in the C-terminal PH region of VPS13A

(**A**) Amino acid sequence of the C-terminal region (residues 3067–3166) of mouse VPS13A. The β-strand and α-helical regions are highlighted in red and green, respectively. The residues involved in hydrophobic interactions are boxed. (**B**) AlphaFold 3-predicted tertiary structure of mouse VPS13A. The β-strand and α-helix in the C-terminal PH region are shown in red and green, respectively. (**C**) Hydrophobic interactions between the β-strand and α-helix. I3152 in the α-helix interacts with V3071 in the β-strand, and L3153 in the α-helix interacts with I3114 and L3120 in the β-strand, respectively.

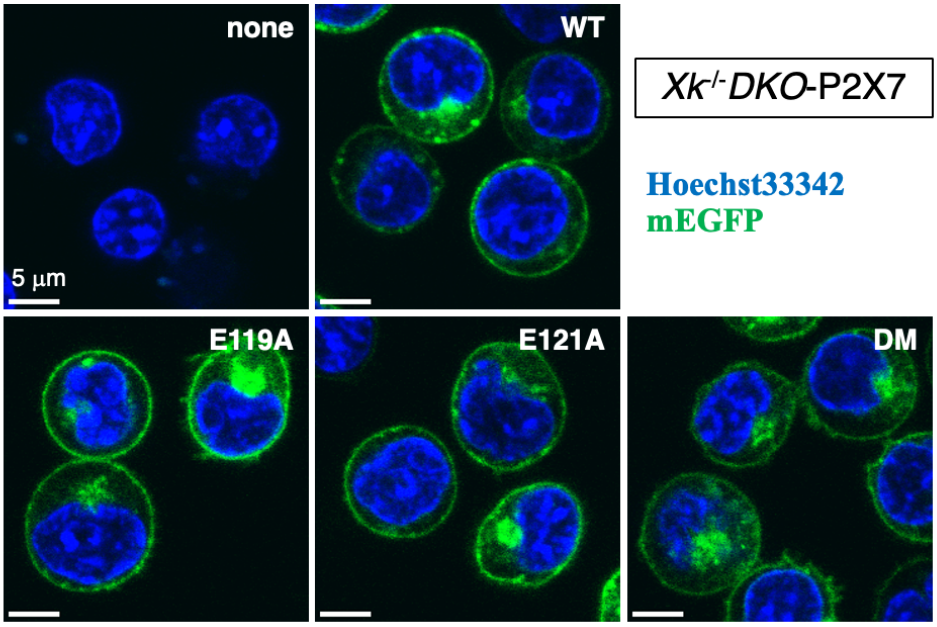

Figure S3. Plasma membrane localization of XK mutants

Xk$^{-/-}$*DKO*-P2X7 cell and its transformants expressing C-terminally mEGFP-tagged mouse XK [WT, E119A, E121A, or DM (E119A/E121A)] were analyzed by confocal fluorescence microscopy.



Figure S4. Amino acid sequence alignment of the mouse XKR family

The amino acid sequences of mouse XK (UniProt, Q9QXY7), XKR2 (UniProt, Q5GH68), and XKR8 (UniProt, Q8C0T0) were aligned to obtain maximal homology by introducing gaps (-). The putative transmembrane regions in XK are shaded. The β-hairpins in XK and XKR2 are highlighted in yellow. The residues that are identical between XK and XKR2 or among all three members are indicated in red. The caspase recognition site in XKR8 is underlined.

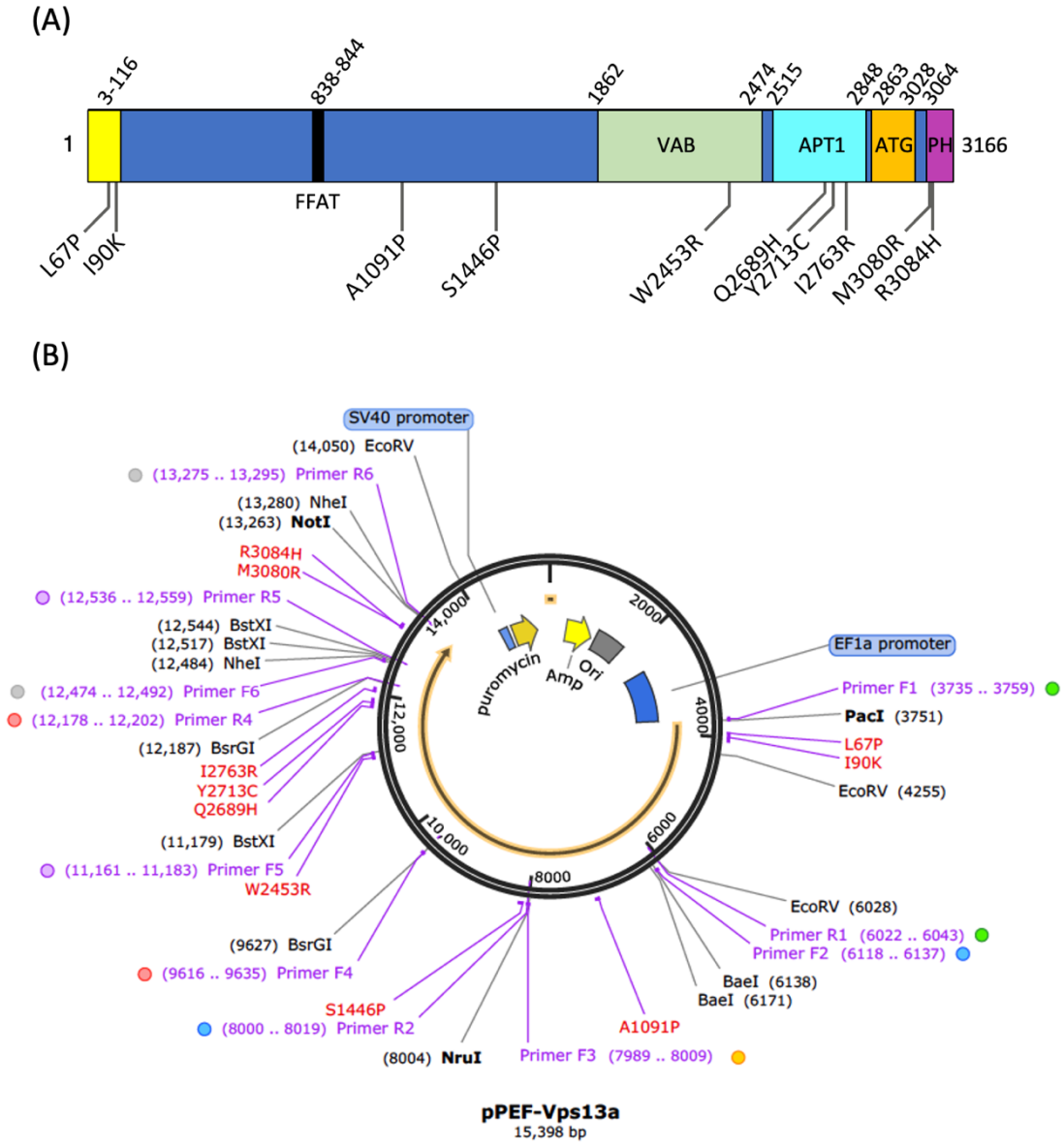

Figure S5. Expression vector construction for mouse VPS13A mutants

(legend on next page)

(**A**) Schematic representation of the domain structure of the mouse VPS13A. The N-terminal Chorein_N (aa 3–116), VAB (VPS13 adaptor binding, aa 1862–2474), APT1 (aberrant pollen transmission 1 domain, aa 2515–2848), ATG_C (autophagy C-terminal, aa 2863–3028), and PH (pleckstrin homology, aa 3064–3166) domains are shown. The FFAT motif (two phenylalanine in an acidic tract, aa 838-844) is also shown. The positions of point mutations introduced into mouse VPS13A are indicated. (**B**) Construction strategy for the mutant expression vectors. A 9,498 bp DNA fragment encoding mouse VPS13A, preceded by a Kozak sequence, was inserted between the PacI and NotI sites of pPEF-BOS-EX vector. Ten missense mutants (L67P, I90K, A1091P, S1446P, W2453R, Q2689H, Y2713C, I2763R, M3080R, and R3084H) are highlighted in red. The forward (F1–F6) and reverse (R1–R6) primers used for PCR mutagenesis are shown in purple. Restriction enzyme sites (PacI, EcoRV, BaeI, NruI, BsrGI, BstXI, and NheI) used for In-Fusion cloning are indicated by their nucleotide positions.

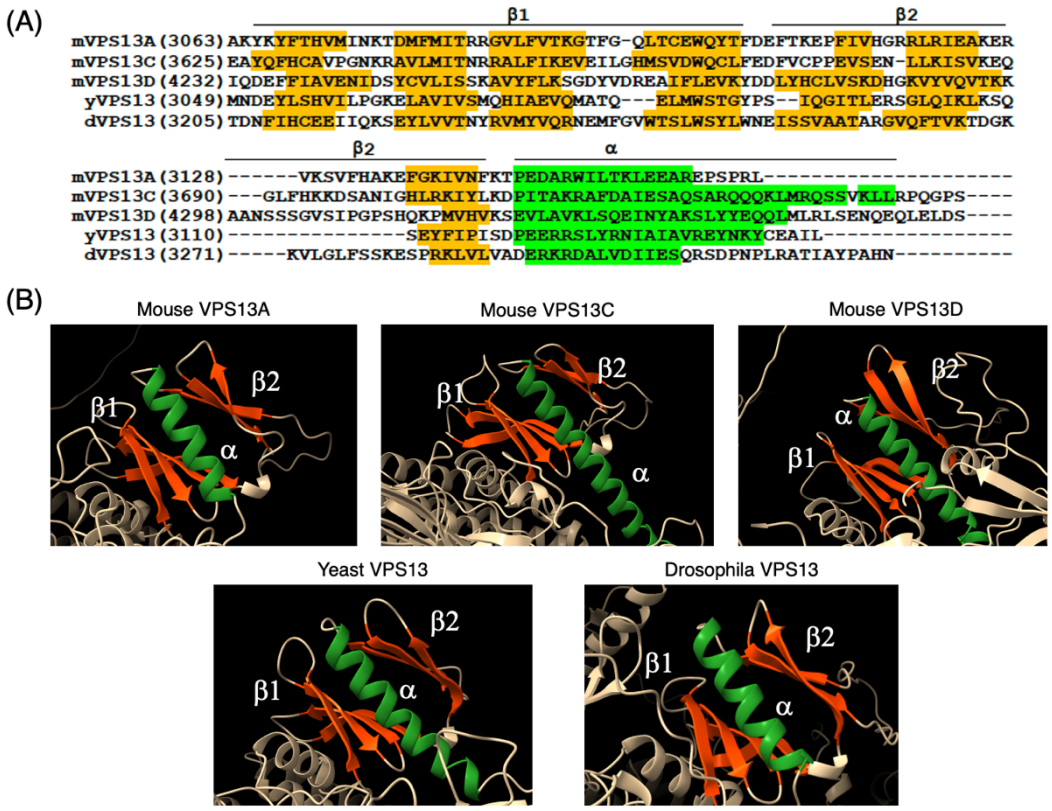

Figure S6. The conserved C-terminal region of the VPS13 family

(**A**) Amino acid sequences of the C-terminal regions of mouse VPS13A (UniProt: Q5H8C4), VPS13C (UniProt: Q8BX70), VPS13D (UniProt: B1ART2), *S. cerevisiae* VPS13 (UniProt Q07878), and *Drosophila* VPS13 (UniProt: A1Z713) were aligned. Two clusters of β-strands (β1 and β2) and α-helix are highlighted in orange and green, respectively. (**B**) AlphaFold 3-predicted β–α–β structure of mouse VPS13A, VPS13C, VPS13D, *S. cerevisiae* VPS13, and *Drosophila* VPS13. The α-helix and β-strands are shown in green and red, respectively.

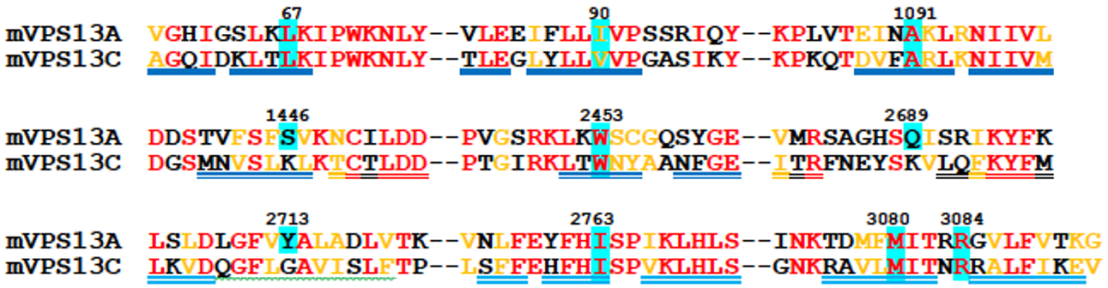

Figure S7. Conservation of essential residues between VPS13A and VPS13C

The amino acid sequence surrounding the mutated 10 residues (highlighted in sky blue with the residue number above the line) of mouse VPS13A (UniProt: Q5H8C4) was aligned with the corresponding region of mouse VPS13C (UniProt: Q8BX70). Identical residues between the two proteins are shown in red, and residues belonging to the same physicochemical categories (nonpolar: G, A, V, I, L, P, F, W, and M; uncharged polar: S, T, C, Y, Q, and N; charged polar: D, E, K, R, and H) are shown in orange. β-strand regions are indicated by double underlines, and α-helical regions are indicated by wavy underlines.

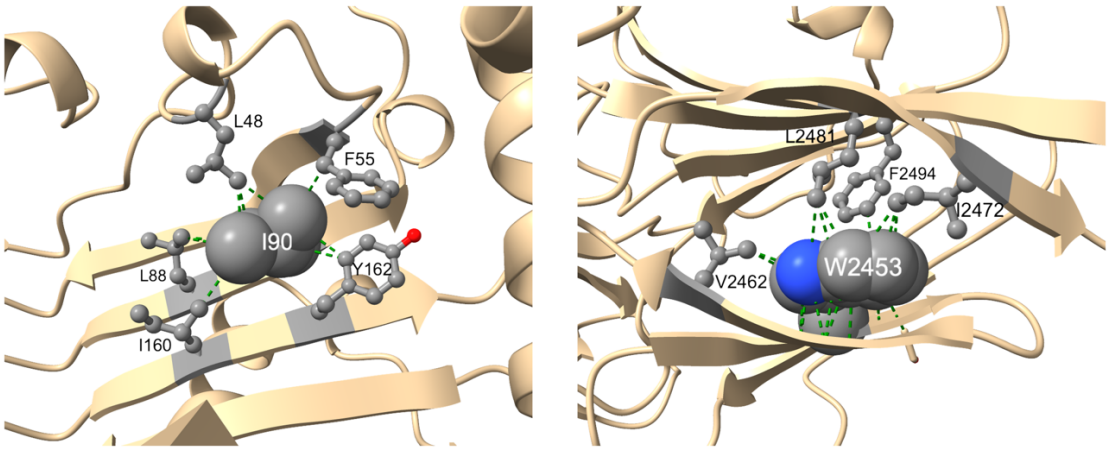

Figure S8. Strong hydrophobic interaction I90 and W2453 with surrounding residues

The local structures of I90 and W2453 in mouse VPS13A are shown. The residues interacting with I90 and W2453 were predicted using the Contact Command of ChimeraX and are shown as colored elements.

9. Supplementary Tables

Table S1. Primers used for deleting mCherry from human VPS13A^mCherry

	Forward primer	Reverse joint primer
upstream fragment	5'-TGTTTTAATGTAAATGCTCAG (BlpI)	5'-CCACAGTTGCTCCTCCTGAATGGTGTGAAG

	Forward joint primer	Reverse primer
downstream fragment	5'-TTCAGGAGGAGCAACTGTGGTGACAGCTGC	5'- CTTATAATATTCTCCAATTTAAATTC (SwaI)

*1 The recognition sites for restriction enzyme (BlpI and SwaI) in the forward and reverse primers are underlined.

*2 The complementary region in the reverse and forward mutagenesis primers are underlined.

Table S2. Primers used for mutagenesis of mouse VPS13A

Mutagenesis Primers for mouse VPS13A mutants

mutant	forward primer	reverse mutagenesis primer	forward mutagenesis primer	reverse primer
L67P	Primer_F1	5'-ATTTTAgGTTTAAGACTACCTATATGACCAAC-3'	5'-TCTTAAACcTAAAATTCCATGGAAAAACCTTT-3'	Primer_R1
I90K	Primer_F1	5'-GGCACTtTGAGTAAAAAAATTTCTTCCAAAAC-3'	5'-TTTACTCAaAGTGCCTTCTTCTAGAATACAG-3'	Primer_R1
A1091P	Primer_F2	5'-GCTTTGgATTTATTTCAGTGACTAGAGGTTTC-3'	5'-AAATAAATcCAAAGCTAAGGAATATAATTGTG-3'	Primer_R2
S1446P	Primer_F3	5'-TTACTGgGAAAGAAAAGACTGTAGAATCATCT-3'	5'-TTTCTTTCcCAGTAAAAAACTGTATTTTAGATGA-3'	Primer_R4
W2453R	Primer_F4	5'-AGCTCCtCTTCAGCTTTCTAGAGCCCACTGG-3'	5'-AGCTGAAGaGGAGCTGTGGGCAAAGCTATGG-3'	Primer_R4
Q2689H	Primer_F5	5'-TGATATgTGGGAATGTCCTGCAGATC-3'	5'-CATTCCCAcATATCACGCATTAAGTATTTCAAAG-3'	Primer_R5
Y2713C	Primer_F5	5'-AGGGCAcACACAAATCCAAGATCCAAACTGAG-3'	5'-ATTTGTGTgTGCCCTAGCAGACCTTGTCAC-3'	Primer_R5
I2763R	Primer_F5	5'-GGAGATcTATGAAAATATTCAAAGAGATTGACTTGTG-3'	5'-TTTTCATAgATCTCCTATCAAGTTGCACTTGAG-3'	Primer_R5
M3080R	Primer_F6	5'-GTTATCcTGAACATATCTGTTTTATTGATCAT-3'	5'-TATGTTCAgGATAACAAGACGTGGCGT-3'	Primer_R6
R3084H	Primer_F6	5'-tGTCTTGTTATCATGAACATATCTGTTTTATTGATCATG-3'	5'-CATGATAACAAGACaTGGCGTGTTGTTCGTAACAAAGG-3'	Primer_R6
R3127*	Primer_F6	5'-TTCACtcaTTCCTTGGCTTCAATGCGC-3'	5'-CAAGGAAtgaGTGAAGTCTGTATTCCATGCC-3'	Primer_R6
E3136*	Primer_F6	5'-TTCCAAA^CTTTGGCATGGAATACAGACTTCA-3'	5'-TGCCAAAG^TTTGGAAAAATCGTTAACTTCAAGA-3'	Primer_R6

* Complementary sequences are underlined, while mutated nucleotides are shown in lower case letters.

Forward and reverse junction primers

Junction Primers			
Primer_F1	5'-CGTGAGGAATTCTTAATTAAGCCAC-3' (PacI)	Primer_R1	5'-TTTGGGCATCTTGATATCCATG-3' (EcoRV)
Primer_F2	5'-GTTGGGAAGCATTCCAAAGC-3'	Primer_R2	5'-TCCAGAGAAGGATCGCGAAC-3' (NruI)
Primer_F3	5'-CCTTTACAGATGTTCGCGATC-3' (NruI)		
Primer_F4	5'-GGGACGCCGTCTGTACACTG-3' (BsrGI)	Primer_R4	5'-AACTACATCTTGTACATCTGTGAGG-3' (BsrGI)
Primer_F5	5'-TATGATGACGCCCATAAGTGTGG-3' (BstXI)	Primer_R5	5'-GTAGTCTTCATCCATGGTCATGGC-3' (BstXI)
Primer_F6	5'-CCGTTGGTGGGCTAGCTGG-3' (NheI)	Primer_R6	5'-TAGAGTCGACGCTAGCGGATC-3' (NheI)

* The recognition site for restriction enzyme is underlined.

Table S3. Primers used for mutagenesis of mouse XK

Mutagenesis Primers for XK mutants

mutant	forward primer	reverse mutagenesis primer	forward mutagenesis primer	reverse primer
E119A	Primer_F7	5'-TCTTTCgCCACCTCCTCTGAAAGGCC-3'	5'-GGAGGTGGcGAAAGAGGTTGGCCAGGC-3'	Primer_R7
E121A	Primer_F7	5'-CCAACCgCTTTCTCCACCTCCTCTGAAAGGC-3'	5'-GGAGAAAGcGGTTGGCCAGGCAGAAGG-3'	Primer_R7
E119A/E121A	Primer_F7	5'-CCAACCgCTTTCgCCACCTCCTCTGAAAGGCC-3'	5'-GTGGcGAAAGcGGTTGGCCAGGCAGAAGG-3'	Primer_R7

* Complementary sequences are underlined, while mutated nucleotides are shown in lower case letters.

Forward and reverse junction primers

Junction Primers			
Primer_F7	5'-ATATGGATCCGAGATGAAATTCCCGGCCTCGGT-3' (BamHI)	Primer_R7	5'-ATATGAATTCAGCAGAGCACAGATCAACAG-3' (EcoRI)

* The recognition site for restriction enzyme is underlined.

10. References

1. Yang Y, et al. Phospholipid subcellular localization and dynamics. *J Biol Chem.* 2018;293(17):6230-6240.

2. Harayama T, and Riezman H. Understanding the diversity of membrane lipid composition. *Nat Rev Mol Cell Biol.* 2018;19(5):281-296.

3. Vance JE. Phospholipid synthesis and transport in mammalian cells. *Traffic.* 2015;16(1):1-18.

4. Tafesse FG, et al. The multigenic sphingomyelin synthase family. *J Biol Chem.* 2006;281(40):29421-29425.

5. Doktorova M, et al. Cell membranes sustain phospholipid imbalance via cholesterol asymmetry. *Cell.* 2025;188(10):2586-2602.

6. Sakuragi T, and Nagata S. Regulation of phospholipid distribution in the lipid bilayer by flippases and scramblases. *Nat Rev Mol Cell Biol.* 2023;24(8):576-596.

7. Segawa K, et al. Caspase-mediated cleavage of phospholipid flippase for apoptotic phosphatidylserine exposure. *Science.* 2014;344(6188):1164-1168.

8. Segawa K, et al. Human type IV P-type ATPases that work as plasma membrane phospholipid flippases, and their regulation by caspase and calcium. *J Biol Chem.* 2016;291(2):762-772.

9. Bevers EM, and Williamson PL. Getting to the outer leaflet: Physiology of phosphatidylserine exposure at the plasma membrane. *Physiol Rev.* 2016;96(2):605-645.

10. Miyata Y, et al. Membrane structure-responsive lipid scrambling by TMEM63B to control plasma membrane lipid distribution. *Nat Struct Mol Biol.* 2025(32):185-198.

11. Niu H, et al. Phospholipid scrambling induced by an ion channel/metabolite transporter complex. *Nat Commun.* 2024;15(1):7566.

12. Suzuki J, et al. Calcium-dependent phospholipid scrambling by TMEM16F.

Nature. 2010;468(7325):834-838.

13. Suzuki J, et al. Xk-related protein 8 and CED-8 promote phosphatidylserine exposure in apoptotic cells. *Science.* 2013;341(6144):403-406.

14. Gusic M, et al. Dissecting activation steps in P2X7 receptors. *Biochem Biophys Res Commun*. 2021;569:112-117.

15. Di Virgilio F, et al. Extracellular ATP and P2 purinergic signalling in the tumour microenvironment. *Nat Rev Cancer.* 2018;18(10):601-618.

16. Di Virgilio F, et al. The P2X7 receptor in infection and inflammation. *Immunity.* 2017;47(1):15-31.

17. Khakh BS, and North RA. Neuromodulation by Extracellular ATP and P2X Receptors in the CNS. *Neuron*. 2012;76(1):51-69.

18. Shokoples BG, et al. P2X7 Receptors. *Arterioscler Thromb Vasc Biol*. 2021;41(1):186-199.

19. Linden J, et al. Purine Release, Metabolism, and Signaling in the Inflammatory Response. *Annu Rev Immunol*. 2019;37(1):325-347.

20. Koch-Nolte F, et al. Novel biologics targeting the P2X7 ion channel. *Curr Opin Pharmacol*. 2019;47:110-118.

21. Swan LE. VPS13 and bridge-like lipid transporters, mechanisms, and mysteries. *Front Neurosci.* 2025;19:1534061.

22. Peikert K, et al. In: Adam MP, Ardinger HH, Pagon RA, Wallace SE, Bean LJ, Stephens K, et al. eds. *GeneReview*. Seatle, USA: U.S. National Library of Medicine; 2023.

23. Dall'Armellina F, et al. In silico modeling human VPS13 proteins associated with donor and target membranes suggests lipid transfer mechanisms. *Proteins Struct Funct Bioinformat.* 2023;91(4):439-455.

24. Dziurdzik SK, and Conibear E. The Vps13 family of lipid transporters and its role at membrane contact sites. *Int J Mol Sci.* 2021;22(6):2905.

25. Walker RH, et al. Neuroacanthocytosis syndromes: The clinical perspective. *Contact.* 2023;6:1-10.

26. Ledderose C, et al. Optimized HPLC method to elucidate the complex purinergic signaling dynamics that regulate ATP, ADP, AMP, and adenosine levels in human blood. *Purinerg Signal.* 2022;18(2):223-239.

27. Ryoden Y, et al. Requirement of Xk and Vps13a for the P2X7-mediated phospholipid scrambling and cell lysis in mouse T cells. *Proc Nat Acad Sci USA.* 2022;119(7):e2119286119.

28. Urata Y, et al. Novel pathogenic XK mutations in McLeod syndrome and interaction between XK protein and chorein. *Neurol Genet.* 2019;5(3):e328.

29. Park J-S, et al. Interaction between VPS13A and the XK scramblase is important for VPS13A function in humans. *J Cell Sci.* 2022;135(17): jcs260227.

30. Guillén-Samander A, et al. A partnership between the lipid scramblase XK and the lipid transfer protein VPS13A at the plasma membrane. *Proc Natl Acad Sci USA.* 2022;119(35):e2205425119.

31. Park J-S, et al. XK is a partner for VPS13A: a molecular link between chorea-acanthocytosis and McLeod syndrome. *Mol Biol Cell.* 2020;31(22):2425-2436.

32. Abramson J, et al. Accurate structure prediction of biomolecular interactions with AlphaFold 3. *Nature.* 2024;630(8016):493-500.

33. Park J-S, et al. Yeast Vps13 promotes mitochondrial function and is localized at membrane contact sites. *Mol Biol Cell.* 2016;27(15):2435-2449.

34. Zheng C, et al. Structural studies of NF-κB signaling. *Cell Res.* 2011;21(1):183-195.

35. Watkins AM, and Arora PS. Anatomy of β-strands at protein–protein interfaces. *ACS Chem Biol.* 2014;9(8):1747-1754.

36. Estes, B, et al. Uncovering methods for the prevention of protein aggregation and improvement of product quality in a transient expression system. *Biotechnol Prog.* 2015;31(1):258-267.

37. Kageyama Y, et al. A new phenotype of chorea-acanthocytosis with dilated cardiomyopathy and myopathy. *Mov Disord.* 2007;22(11):1669-1670.

38. Dobson-Stone C, et al. Mutational spectrum of the CHAC gene in patients with chorea-acanthocytosis. *Eur J Hum Genet.* 2002;10(11):773-781.

39. Heuberger EH, et al. Oligomeric state of membrane transport proteins analyzed with blue native electrophoresis and analytical ultracentrifugation. *J Mol Biol.* 2002;317(4):591-600.

40. Suzuki J, et al. Exposure of phosphatidylserine by Xk-related protein family members during apoptosis. *J Biol Chem.* 2014;289(44):30257-30267.

41. Suzuki J, et al. Xkr8 phospholipid scrambling complex in apoptotic phosphatidylserine exposure. *Proc Nat Acad Sci USA.* 2016;113(34):9509-9514.

42. Rampoldi L, et al. A conserved sorting-associated protein is mutant in chorea-acanthocytosis. *Nat Genet.* 2001;28(2):119-120.

43. Saiki S, et al. Primary skeletal muscle involvement in chorea-acanthocytosis. *Mov Disord.* 2007;22(6):848-852.

44. Walker RH, et al. Genetic diagnosis of neuroacanthocytosis disorders using exome sequencing. *Mov Disord.* 2012;27(4):539-543.

45. Tomiyasu A, et al. Novel pathogenic mutations and copy number variations in the VPS13A gene in patients with chorea-acanthocytosis. *Am J Med Genet B, .* 2011;156(5):620-631.

46. Chaudhari S, et al. Exome sequencing of choreoacanthocytosis reveals novel mutations in VPS13A and co-mutation in modifier gene(s). *Mol Genet Genomics.* 2023;298(4):965-976.

47. Fromer M, et al. De novo mutations in schizophrenia implicate synaptic networks. *Nature.* 2014;506(7487):179-184.

48. Mizushima S, and Nagata S. pEF-BOS, a powerful mammalian expression vector. *Nucleic Acids Res.* 1990;18(17):5322.

49. Cadart C, et al. Size control in mammalian cells involves modulation of both

growth rate and cell cycle duration. *Nat Commun.* 2018;9(1):3275.

50. Zatulovskiy E, and Skotheim JM. On the Molecular Mechanisms Regulating Animal Cell Size Homeostasis. *Trends Genet.* 2020;36(5):360-372.

51. Takahashi M, et al. Amphipathic fluorescent dyes for sensitive and long-term monitoring of plasma membranes. *bioRxiv.* 2020.

52. Reinisch KM, et al. Lipid Dynamics at Membrane Contact Sites. *Annu Rev Biochem.* 2025;94(1):479-502.

53. Kumar N, et al. VPS13A and VPS13C are lipid transport proteins differentially localized at ER contact sites. *J Cell Biol.* 2018;217(10):3625-3639.

54. Ueno S-i, et al. The gene encoding a newly discovered protein, chorein, is mutated in chorea-acanthocytosis. *Nat Genet.* 2001;28(2):121-122.

55. Lesage S, et al. Loss of VPS13C Function in autosomal-recessive Parkinsonism causes mitochondrial dysfunction and increases PINK1/Parkin-dependent mtophagy. *Am J Hum Genetics.* 2016;98(3):500-513.

56. Seong E, et al. Mutations in VPS13D Lead to a New Recessive Ataxia with Spasticity and Mitochondrial Defects. *Ann Neurol.* 2018;83(6):1075-1088.

57. Kolehmainen J, et al. Cohen syndrome is caused by mutations in a novel gene, COH1, encoding a transmembrane protein with a presumed role in vesicle-mediated sorting and intracellular protein transport. *Am J Hum Genet.* 2003;72(6):1359-1369.

58. Xu P, et al. Impaired hematopoiesis and embryonic lethality at midgestation of mice lacking both lipid transfer proteins VPS13A and VPS13C. *PLoS Biol.* 2025;23(9):e3003393.

59. Rzepnikowska W, et al. Yeast and other lower eukaryotic organisms for studies of Vps13 proteins in health and disease. *Traffic.* 2017;18(11):711-719.

60. Rzepnikowska W, et al. Amino acid substitution equivalent to human chorea-acanthocytosis I2771R in yeast Vps13 protein affects its binding to phosphatidylinositol 3-phosphate. *Hum Mol Genet.* 2017;26(8):1497-1510.

61. Park J-S, and Neiman AM. VPS13 regulates membrane morphogenesis during sporulation in Saccharomyces cerevisiae. *J Cell Sci.* 2012;125(12):3004-3011.

62. Bankaitis VA, et al. Isolation of yeast mutants defective in protein targeting to the vacuole. *Proc Natl Acad Sci USA.* 1986;83(23):9075-9079.

63. Vonk JJ, et al. Drosophila Vps13 is required for protein homeostasis in the brain *PLoS ONE.* 2017;12(1):e0170106.

64. Davalos D, et al. ATP mediates rapid microglial response to local brain injury in vivo. *Nat Neurosci.* 2005;8(6):752-758.

65. Birge RB, et al. Phosphatidylserine is a global immunosuppressive signal in efferocytosis, infectious disease, and cancer. *Cell Death Differ.* 2016;23:962-978.

66. Ditzel RM, et al. An autopsy series of seven cases of VPS13A disease (chorea-acanthocytosis). *Mov Disord.* 2023;38(12):2163-2172.

67. Lang AB, et al. ER–mitochondrial junctions can be bypassed by dominant mutations in the endosomal protein Vps13. *J Cell Biol.* 2015;210(6):883-890.

68. Smith M, et al. ER–plasma membrane contact sites deliver ER lipids and proteins for rapid cell surface expansion. *J Cell Biol.* 2024;223(12):e202308137.

69. Fujisawa A, et al. Chemical profiling of the endoplasmic reticulum proteome using designer labeling reagents. *J Am Chem Soc.* 2018;140(49):17060-17070.

70. Morita S, et al. Plat-E: an efficient and stable system for transient packaging of retroviruses. *Gene Ther.* 2000;7(12):1063-1066.

71. Ryoden Y, et al. Functional expression of the P2X7 ATP receptor requires Eros. *J Immunol.* 2020;204(3):559-568.

72. Sadaie W, et al. Quantitative in vivo fluorescence cross-correlation analyses highlight the importance of competitive effects in the regulation of protein-protein interactions. *Mol Cell Biol.* 2014;34(17):3272-3290.

73. Cong L, et al. Multiplex genome engineering using CRISPR/Cas systems. *Science.* 2013;339(6121):819-823.

74. Ran FA, et al. Genome engineering using the CRISPR-Cas9 system. *Nat Protoc.* 2013;8(11):2281-2308.

75. Pachitariu M, et al. Cellpose-SAM: superhuman generalization for cellular segmentation. *bioRxiv.* 2025.

76. Meng EC, et al. UCSF ChimeraX: Tools for structure building and analysis. *Protein Science.* 2023;32(11):e4792.

11. Research achievements

1. Xing Lin, Yuta Ryoden, Chigure Suzuki, Hiroyuki Ishikawa, Takaharu Sakuragi, Yasuo Uchiyama, Shigekazu Nagata. Four types of VPS13A missense mutations for *VPS13A* disease. *J Clin Invest.* In revision.
2. Xing Lin. XK-VPS13A Complex Is Essential for ATP-Stimulated Scramblase Activity. The 637th RIMD Seminar. 2025-06-24.
3. Xing Lin. Four types of missense mutations in the *VPS13A* gene for *VPS13A* disease. The 5th Cell Death Colloquium. 2026-01-09.

12. Acknowledgements

I would like to show my sincere gratitude to my supervisor, Professor Shigekazu Nagata, Ph.D., at Immunology Frontier Research Center (IFReC), The University of Osaka (UOsaka), for his invaluable guidance, insightful suggestions, and inspirational encouragement, which were indispensable for my research. I am also deeply grateful to Mr. Hiroyuki Ishikawa and Assistant Professor Takaharu Sakuragi, Ph.D. (IFReC, UOsaka) for their consistent guidance on experiments and constructive comments in discussions. I am thankful to Mr. Yuta Ryoden, Ph.D. (IFReC, UOsaka; presently at Otsuka Pharmaceutical Co., Ltd.) for his initial study on VPS13A-XK interactions and providing me with plasmids, cell lines and experimental protocols. Special thanks to Specially Appointed Associate Professor Chigure Suzuki, Ph.D. and Specially Appointed Professor Yasuo Uchiyama, Ph.D. at Graduate School of Medicine, Juntendo University, for their help to obtain the transmission electron microscopy data. Finally, I also thank Ms. Masako Harayama and Ms. Mayu Kamada for secretarial assistance.